

The author(s) shown below used Federal funds provided by the U.S. Department of Justice and prepared the following final report:

Document Title: A HAND-HELD DNA-BASED FORENSIC TOOL

Author: Carl A. Batt, Scott J. Stelick, Matthew J. Kennedy, Clarissa S. Lui, Adam J. Lowe

Document No.: 227499

Date Received: July 2009

Award Number: 2004-DN-BX-K001

This report has not been published by the U.S. Department of Justice. To provide better customer service, NCJRS has made this Federally-funded grant final report available electronically in addition to traditional paper copies.

Opinions or points of view expressed are those of the author(s) and do not necessarily reflect the official position or policies of the U.S. Department of Justice.

A HAND-HELD DNA-BASED FORENSIC TOOL

Award Number: #2004-DN-BX-K001

Carl A. Batt, Scott J. Stelick, Matthew J. Kennedy, Clarissa S. Lui, Adam J. Lowe

Abstract

Genomics promises to enable a new class of tools for rapid field-based forensics when combined with emerging lab-on-a-chip platforms and molecular probing technologies. Single Nucleotide Polymorphisms (SNPs) are genetic indicators potentially useful for developing phenotypic profiles of individual based on field-acquired DNA samples. Here, we report on 4-years of research and development focused on enabling technologies for portable biosensors in particular for the detection of SNPs.

A fully-portable testing platform was developed for demonstrating our PCR-based detection microchip technology. This prototype instrument was delivered to the NYSP Forensic Investigation Center in June 2005. The system was evaluated by the State Police for a period of 4 months and was tested using a variety of forensic DNA samples. In their evaluation of our technology, the State Police stressed the need to simultaneously detect a large number of SNP targets in a single reaction. In subsequent work, we developed a multiplexing instrument featuring spectral optics and multiplexed molecular labels, and we explored two additional platforms to achieve higher multiplexing capability. In addition, we developed novel microfabricated fluid pumps that are driven by low voltages and can be readily integrated into lab-on-a-chip devices. These novel pumps promise to eliminate all reagent handling duties presently performed by the end user, and our work will enable portable biosensors that accept disposable cartridges pre-loaded with reagents.

One additional platform we developed was a fluorescence-activated particle counter microchip for multiplexed scoring of DNA targets. We constructed and characterized a flow-cell element that guides microparticles into a tightly focused stream for optical interrogation. By adjusting the rates of the focusing fluids, the focused sample was positioned first near the top of the microchannel and then translated down in steps to the bottom of the microchannel (Kennedy, submitted). Furthermore, all of the optics necessary for interrogating the beads was integrated into the microchip. The total run-time from sample-loading to 10,000-event result was approximately 5-minutes. Simultaneous two-color detection of microspheres was demonstrated at a rate of 100-per-second, and over 95% of photon-burst events were shown to correspond to single-bead events.

Much of our work focused on the use of quantum dots as molecular probes. Specifically, we explored the use of quantum dots as molecular beacons and compared the effectiveness of alternative linkage strategies and fluorescence quenchers in hybridization-based assays (Cady N. A., 2007). Amide-linked beacons showed a 57% greater fluorescence increase than streptavidin-linked beacons when hybridized to 200 pmol of target DNA. Measurements of the hydrodynamic radius of the molecular beacon – dna complexes indicated that the larger radius of the streptavidin QDs (13.5 nm) than the carboxyl QDs (7 nm) may have a negative effect on FRET-based quenching for QD molecular beacons.

We demonstrated a new approach to SNP detection through the application of Surface Enhanced Raman Scattering (SERS) to the Ligase Detection Reaction (LDR) (Huh Y. L., Accepted). By detecting the Raman signature of the dye rather than its fluorescence emission, our technique avoids the problem of spectral overlap which limits

number of reactions which can be carried out in parallel by fluorescence-based systems. The reaction uses two LDR primers, one of which contains a Raman enhancer and the other a reporter dye. In LDR, one of the primers is designed to interrogate the SNP. When the SNP being interrogated matches the discriminating primer sequence, the primers are ligated and the enhancer and dye are brought into close proximity enabling the dye's Raman signature to be detected. We demonstrate the LDR-SERS reaction for the detection of point mutations in the human K-ras oncogene. We report a limit of detection of 20 pM of target DNA with the anticipated specificity engendered by the LDR platform.

Ultimately, we anticipate that several of the technologies we have developed, the PCR-microchip, the particle counter microchip, the molecular beacon labeling protocols, and the LDR-SERS techniques, will be integrated into a unified portable biosensor inclusive of preparation, amplification, and multiplexed optical detection of DNA.

TABLE OF CONTENTS

Executive Summary	6
I. Introduction:.....	9
1.0 Single nucleotide polymorphisms (SNPs)	9
1.1 PCR-based detection microchip	9
1.2 Electrolytic Hydraulic micropump	10
1.3 Integrated Flow Cytometer	11
Flow Cytometer Components	12
Signal Processing	12
Electronic Gating.....	13
Hydrodynamic focusing	13
Integrated Flow cytometer	14
Allele-specific Hybridization Assay	14
1.4 Quantum Dot Molecular Beacons	15
1.5 Ligase Detection Reaction with Surface Enhanced Raman Detection	16
II. Methods	18
2.1 PCR-based detection microchip	18
Microchip design and fabrication	18
PCR Amplification	18
MicroFLUIDICS DESKTOP	19
MicroFLUIDICS Desktop MULTIPLEX.....	20
Melting Curve Analysis	20
2.2 Electrolytic Hydraulic micropump	21
Pump Design	21
Electrode Design	21
Pump Filling and Fluid Connections.....	22
Electronic Fluid Control System	22
Gold Electrodes.....	22
2.3 Integrated Flow Cytometer	22

Fabrication	22
Simulations	23
Confocal Microscopy	23
Image Analysis	24
Integrated Flow cytometer	25
Allele-specific SNP Hybridization Assay	27
Optical Barcode for multiplexed detection of DNA	28
2.4 Molecular Beacons	29
Molecular Beacon Design	29
Quantum dot—molecular beacon synthesis	30
Fluorescence measurements and particle sizing	31
Calculation of FRET efficiency	32
2.5 Ligase Detection Reaction with Surface Enhanced Raman Detection	32
Materials	32
LDR reaction	32
LDR functionalization and purification	33
Gel shift assay	33
Microfluidic device	33
Raman spectroscopy measurements	34
III. Results	34
3.1 PCR-based detection microchip	1
MicroFLUIDICS DESKTOP MULTIPLEX	35
Melting Curve Analysis	35
3.2 Electrolytic Hydraulic micropump	36
Testing of Flow Rates	36
Long-Term Testing	36
Pressure Testing	37
Gold Electrode EHP Testing	37
3.3 Integrated Flow Cytometer	38

Manifold Design and Operation	38
Manifold Simulations and Imaging	38
Counting of microspheres	1
Allele specific Hybridization Assay	40
3.4 Quantum Dot Molecular Beacons	41
3.5 Ligase Detection Reaction with Surface Enhanced Raman Detection	43
Description of SERS enhanced LDR reaction.....	43
IV. Conclusions.....	45
4.1 PCR-based detection microchip	45
4.2 Electrolytic Hydraulic micropump	45
4.3 Integrated Flow Cytometer	46
4.4 Quantum Dot Molecular Beacons	47
4.5 Ligase Detection Reaction with Surface Enhanced Raman Detection	50
VI. Dissemination of Research Findings	50
Bibliography.....	50

EXECUTIVE SUMMARY

Genomics provides a comprehensive view of the complete genetic makeup of an organism. Individual sequence variations, as manifested by single nucleotide polymorphisms (SNPs), can provide insight into the basis for a large number of phenotypes. The ability to rapidly screen for SNPs will have a profound impact on a number of applications, including forensics.

The goal of the proposed research was to develop a single portable device capable of both extracting DNA from forensic evidence and scoring for phenotypic traits and SNPs. We collaborated actively with the NYSP Forensic Investigation Center in establishing protocols and appropriate PCR and SNP targets. In addition we worked with Evident Technologies (Troy, NY) to further enhance the potential detection sensitivity using quantum dot labels. The following goals were proposed to develop a portable device to extract DNA from forensic evidence and score it for phenotypic traits/SNPs:

1. Design a PCR-based detection microchip inclusive of preparation, amplification and analysis modules.
2. Fabricate a PCR-based detection microchip.
3. Formulate on-chip fluorescence TaqMan allelic discrimination assay for phenotypic traits and single nucleotide polymorphisms (SNPs).
4. Test detection microchip with DNA lysis/purification module.

We designed and fabricated a PCR-based detection microchip and formatted an on-chip fluorescence TaqMan allelic discrimination assay. Monolithic DNA purification / real-time PCR silicon chips were fabricated and tested for their ability to purify and detect the DNA. Using silica-coated microstructures, nucleic acids could be selectively bound, washed and eluted for subsequent real-time PCR. These microstructures were included in an integrated detection microchip containing two distinct regions, one for DNA purification and one for real-time PCR. Using an automated detection platform with integrated microprocessor, pumps, valves, thermocycler and fluorescence detection modules, microchips were used to purify and detect bacterial DNA by real-time PCR amplification using SYBR Green fluorescent dye.

Recently, we set out to improve the basic fluid-manipulation technology associated with implementing the detection microchip. In particular, we wish to eliminate the cumbersome reagent handling and fluid connection steps required by the instrument operator. To meet this need, we developed electrolytic hydraulic micropumps (μ EHPs). These novel pumps promise to eliminate all reagent handling duties presently performed by the end user, and our work will enable portable biosensors that accept disposable cartridges pre-loaded with reagents.

More recently, we began developing an integrated PCR-based detection Lab on-a-chip. The new integrated microchip contains several components previously implemented by the supporting microFLUIDICS DESKTOP, which are now fabricated into the detection microchip. The technology we are developing will enable the next-generation instrument, which will accept disposable detection cartridges pre-loaded with reagents, relieving the instrument operator from fluid-handling tasks. Integral to this integrated microchip is the Electrolytic Hydraulic Pump (EHP), several of which have been integrated into our microchip. Unlike other pump designs, this design separates the pumped reagents from the electrolyte, which prevents contamination of the pumping fluid. The sizes of the electrolyte and reagent chambers can be modified to provide hydraulic advantage. During testing, we achieved flow rates from 6 to 30 μ l/minute with high pressure (7-16psi), low power consumption (10-72mW), and low voltage (5-12V) compatible with battery powered operation.

We constructed a fully-functional testing platform for our original design of the PCR detection microchip and this was delivered to the NYSP Forensic Investigation Center in June 2005. The system was evaluated by the State Police for a period of 4 months and was tested using a variety of forensic DNA samples. The State Police provided

us with a thorough evaluation of our developed technology and suggested some alternate approaches to developing a multiplex SNP detection assay. From their evaluation, the State Police suggested that we develop a multiplex assay that could detect multiple SNP targets in a single reaction. Unlike the TaqMan or SYBR Green assays that we have demonstrated thus far, we discussed the development of a bead-based assay where amplified DNA targets could be attached to fluorescently labeled beads. After attachment, the beads could be scored for the presence or absence of the appropriate DNA targets, allowing us to analyze multiple targets in a single sample.

In light of the suggestions from the State Police, we proceeded to develop a fluorescence-based particle counter microchip for multiplexed scoring of DNA targets. We developed a protocol for surface-modifying optically-barcoded microspheres with single-stranded probe DNA, and we constructed and characterized a flow-cell element that focuses these particles into a tight stream for optical interrogation. Furthermore, all of the optics necessary for interrogating these beads have been successfully integrated into the flow-cell, eliminating the need for mechanical adjustments that are normally required to optically align particle counter devices.

A microfabricated flow cytometer was developed containing two key components, a fluid-focusing manifold and an optical detection system, both integrated into a unified microchip flow-cell. Optical fibers were imbedded into the flow-cell and were used to guide excitation illumination into the detection region and collect fluorescence from the same region. A fluid-focusing manifold was employed to maneuver particles into the region of the illuminating beam. The device was tested for its ability to specifically detect a particular DNA sequence from a heterogeneous DNA mixture containing two very similar sequences. The two sequences present in the mixture differed by a single nucleotide and were labeled with spectrally independent chromophores. Microspheres specific to one allele were added to the volume, allowed to hybridize, and then pumped into the integrated flow cytometer and scored for events corresponding to one allele or the other. The device and assay were characterized for throughput, run-time, target specificity, and sensitivity. The total run-time from sample-loading to 10,000-event result was approximately 5-minutes.

A microfluidic manifold was designed, fabricated, and tested that hydrodynamically focuses a sample into the center of a microchannel and provides control over the vertical position of the sample via the flow-rates of the focusing fluids. To characterize the focusing action, a mixing experiment was performed in which the sample fluid and focusing fluid contained two different fluorescent dyes. The concentration distributions were computed using multiphysics software, and images were obtained using confocal microscopy. By adjusting the rates of the focusing fluids, the focused sample was positioned first near the top of the microchannel and then translated down in steps to the bottom of the microchannel. The simulations were observed to accurately predict the vertical position of the center-of-mass of the focused sample as the ratio of the top focusing fluid to the rate of the bottom focusing fluid was swept over a range of four-orders of magnitude.

Quantum dot (QD) molecular beacons were explored for sequence-specific DNA detection. The effectiveness of multiple linkage strategies and fluorescence quenchers were compared in hybridization-based assays. To compare linkage strategies, covalent amide linkage and streptavidin-biotin binding were used to link semiconductor QDs to molecular beacon DNA. Amide-linked beacons showed a 57% greater fluorescence increase than streptavidin-linked beacons when hybridized to 200 pmol of target DNA. The specificity of the molecular beacons, however, was similar for both linkage methods. Hybridization of both QD molecular beacons with non-complementary target DNA resulted in approximately 50% lower fluorescence intensity than hybridization with complementary DNA. The effectiveness of different quencher moieties was also evaluated. Iowa Black and 1.4 nm Nanogold-quenched molecular beacons exhibited approximately 2-fold greater fluorescence increases than dabcy-quenched beacons when hybridized to complementary target. Specificity for target DNA was also confirmed through hybridization assays with non-complementary DNA. To provide insight into differences between the QD molecular beacons and the linkage strategies used, the hydrodynamic radius of each was measured. These measurements indicated that the larger radius of the streptavidin QDs (13.5 nm) than the carboxyl QDs (7 nm) could have a negative effect on FRET-based quenching for QD molecular beacons. These data outline the

importance of choosing proper linkage methods and quencher moieties for creating high quality QD molecular beacons.

We demonstrated a new approach to SNP detection through the application of Surface Enhanced Raman Scattering (SERS) to the Ligase Detection Reaction (LDR). The reaction uses two LDR primers, one of which contains a Raman enhancer and the other a reporter dye. In LDR, one of the primers is designed to interrogate the SNP. When the SNP being interrogated matches the discriminating primer sequence, the primers are ligated and the enhancer and dye are brought into close proximity enabling the dye's Raman signature to be detected. By detecting the Raman signature of the dye rather than its fluorescence emission, our technique avoids the problem of spectral overlap which limits number of reactions which can be carried out in parallel by existing systems. We demonstrate the LDR-SERS reaction for the detection of point mutations in the human K-ras oncogene. The reaction is implemented in an electrokinetically active microfluidic device that enables physical concentration of the reaction products for enhanced detection sensitivity and quantization. We report a limit of detection of 20 pM of target DNA with the anticipated specificity engendered by the LDR platform.

I. INTRODUCTION:

1.0 SINGLE NUCLEOTIDE POLYMORPHISMS (SNPs)

Single Nucleotide Polymorphisms (SNPs) are single base pair differences in DNA amongst individuals where the less common variant occurs in at least 1% of the total population (Wang, 1998). The decoding of the human genome has revealed more than 3 million SNPs - roughly 1 every 100-300 bases [1]. Single nucleotide polymorphisms (SNPs) are heralded as the genetic markers with the greatest potential for highly efficient and precise identification and description of individuals [2]. SNPs have two characteristics that make them more favorable than the single tandem repeats (STRs) typically used in forensics. First, they have very low mutation rates, making them ideal for use in paternity testing. Second, the fact that they can be analyzed in short amplicons makes them amenable to high throughput technologies such as microarrays, minisequencing [3] and allele-specific primer extension [4].

To make good use of these discoveries, faster and cheaper technological methods are needed to discover new SNPs, for genotyping them in many individuals, and also for clinical diagnostics. All allele-specific SNP discrimination techniques suitable for high throughput genetic analysis can be categorized as: primer extension, oligonucleotide ligation, invasive cleavage or hybridization based (Kwok, 2001). There are numerous variants on the primer extension technique however all are based on the ability of DNA polymerase to incorporate specific deoxyribonucleotides that are complementary to the sequence of the template DNA (Sobrino, 2005). A detailed review of all the implementations is beyond the scope of what can be covered here (see recent reviews by Perkel[5] or Kim and Misra[6] for details) but of the various methods Real-Time PCR or RT-PCR [7-9] is likely of the simplest. The primary reason for this is that the reaction is carried out in a homogenous format and requires no post-PCR processing. This reduces the time and labor required for analysis while minimizing the number of potential sources of error and contamination.

1.1 PCR-BASED DETECTION MICROCHIP

Biosensors have been developed utilizing a variety of existing semiconductor processing strategies. The resulting devices, collectively known as lab-on-a-chip devices, incorporate multiple laboratory processes in a

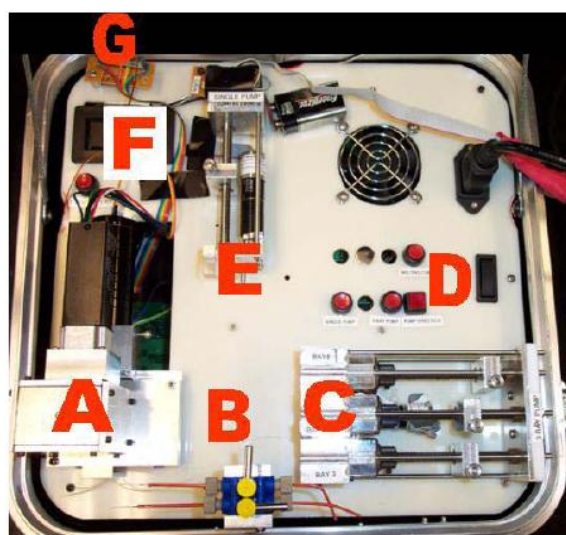
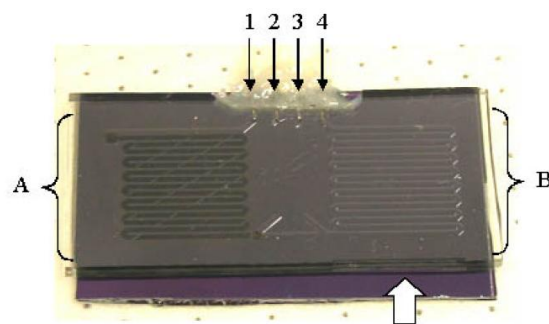


Figure 1: DNA purification/detection microchip and microFLUIDICS DESKTOP. Top: The purification region is denoted “A”, while the real-time PCR detection region is denoted as “B”. Four input/output sources are shown (1-4) as well as a white arrow, denoting the placement of the glass wave guide of the fluorescence detection system. Input 1 is used for introduction of lysate, wash buffer and dH₂O. Input 2 is used as a waste outlet. Bottom: The microFLUIDICS DESKTOP completed in 2005. The system consists of multiple components: A, fluorescence detection system (chip and thermocycler are located below this); B, fluidic valves; C, 3-bay syringe pump; D, electronic switches; E, single-bay syringe pump; F, fluorescence gain display; G, temperature control resistors.

semi-automated, miniaturized format. Many of these devices utilize the polymerase chain reaction (PCR) which is relatively robust, however, a variety of contaminants can inhibit amplification and diminish the success of such analytical instruments [10]. In order to circumvent this problem, DNA must be extracted and purified from a sample through a variety of lysis protocols and purification techniques [11]. In a previous study, our laboratory demonstrated effective bacterial cell lysis and DNA purification in a microfabricated silicon chip [12]. Using a guanidinium thiocyanate-based lysis buffer, DNA was extracted from bacteria and selectively bound to silica-coated microstructures. After a series of washing steps, the purified DNA was then eluted from the chip and utilized for PCR amplification.

Successful chip-based DNA purification and PCR requires not only manufacturing of the detection microchips, but also development of a platform to perform the necessary thermal cycling, fluorescent measurement and fluid control systems. In previous studies, several strategies have been used to fulfill these requirements. For PCR thermal cycling, groups have employed multiple techniques, including infrared light [13], thermoelectric heater-coolers [14], and resistive electrodes [15].

PCR-based detection microchip was fabricated in 2005-6 (**Figure 1**). The base portion of the chip is fabricated in silicon, while the upper portion of the chip (containing the PCR amplification chamber and microfluidic channels) is fabricated from molded polydimethylsiloxane (PDMS). These microchips were delivered (as well as a testing platform) to the New York State Police Forensic Investigation Center for evaluation for evaluation of real-time PCR assays on our microchips.

Upon fabricating the PCR-based detection microchip, it became clear that a testing station was needed for evaluation of the chip performance. In 2005 we designed and constructed a microFLUIDICS DESKTOP for evaluation of the PCR-based microchips. The desktop instrument contained fluid valves and syringe pumps, a fluorescence detection system, and a temperature control and thermocycling system. This platform, along with a complete user manual, was delivered to NYSPFIC and allowed them to evaluate our detection microchip and instrumentation independently.

1.2 ELECTROLYTIC HYDRAULIC MICROPUMP

Progress in biosensor portability has been limited in part by the challenges associated with moving the fluids through the system. For bench-top applications, precise fluid control is often achieved with syringe pumps due to their high precision and ease of use. In addition to syringe pumps, groups have reported on the use of electroosmotic pumps [16], miniaturized peristaltic pumps [17] and thermally-driven pumps [18]. Electroosmotic pumps are intrinsically simple with few moving parts, but are highly dependent upon the geometry of the microchannels [19] and the chemical composition of the fluid to be pumped [20]. Both thermal and electroosmotic pumps are subject to bubble formation from thermal and electrolytic effects, respectively [17]. Bubbles scatter light and can reduce the sensitivity of an instrument relying on optical detection. Miniaturized peristaltic pumps offer an alternative pumping strategy, but require complicated gas control systems for actuating the microfluidic valves. Furthermore, these systems can be overly cumbersome for integration into a portable detection system.

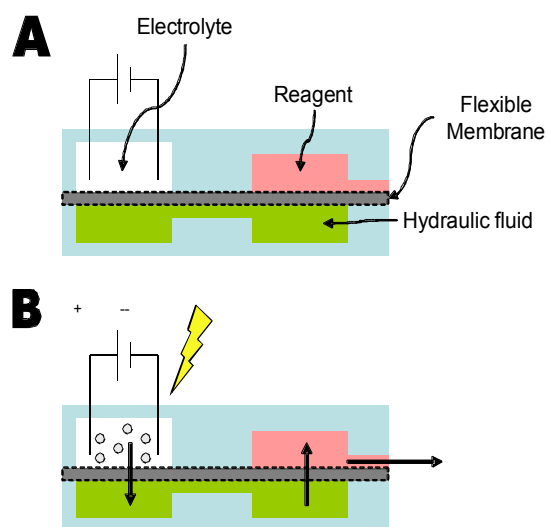


Figure 2. The Electrolytic Hydraulic Pump (EHP). Pumping fluid (electrolyte) is subjected to an electrical current, causing bubble formation through electrolysis. Pressure is transferred to a hydraulic fluid through a flexible membrane, which then forces fluid out of the reagent reservoir.

In order to develop portable biosensor instruments that accept disposable flow-cell cartridges pre-loaded with reagents, we have developed novel microfabricated hydraulics-based fluid pumps. These μ EHPs are a foundation technology that will enable portable biosensors for a variety of applications. The goal is to use μ EHP pumps in an integrated system for a complete PCR detection system. The actuation of the pump does not require larger external devices and the pumps as well as the associated electronics can be scaled dramatically. Unlike other pump designs, this design separates the pumped reagents from the electrolyte, which prevents contamination of the pumping fluid. This is especially important for biological and chemical applications. This innovative design can also provide higher pressure than traditional pumps.

The basic EHP design consists of two pumping chambers that separately contain pumping fluid (electrolyte) and liquid reagents. Electrodes are placed in the electrolyte chamber (EC) and gas bubbles are produced via electrolysis when a voltage is applied. The increased pressure within the EC chamber due to the generation of gas bubbles is transferred to the fluid in the hydraulic chamber (HC) via a thin flexible membrane (**Figure 2**). The HC is split into two effective chambers, one that responds to the EC and that actuates the reagent chamber (RC). The pressure applied to the hydraulic fluid from the EC is translated to the RC, forcing the reagent to move through an outlet. In this way, small amounts of electrical energy can be used to pump fluids in a controlled manner.

Several EHP pumps were integrated onto a single chip inclusive of a purification and amplification chamber. The goal of this particular effort was to explore the potential for developing an integrated PCR-based lab on-a-chip (PCR-LC), as shown in **Figure 3**. This central design concept of the PCR-LC is a disposable cartridge that can be quickly inserted and ejected from an accepting instrument and which contains pre-loaded on-chip all reagents necessary for purification and amplification.

1.3 INTEGRATED FLOW CYTOMETER

There is a need for a field-deployable instrument that can detect specific DNA sequences from a heterogeneous mixture of DNA. A field deployable instrument should be compact and portable and the total run-time must be short and require minimal operator intervention. Such a device will find use in environmental microbiology, food safety, and forensic evidence evaluation.

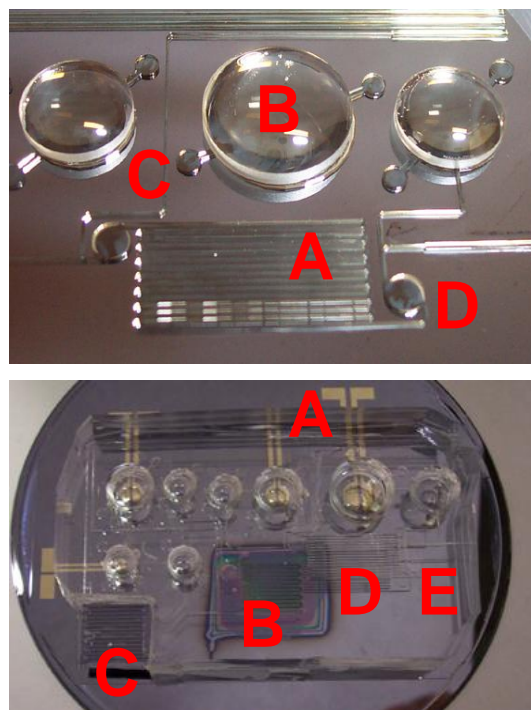


Figure 3 *Integrated PCR-based Lab on-a-Chip (PCR-LC) for SNP Screening.* **Top:** Silicon master for replica-based fabrication of EHP pumps. (A) Fluid channels are fabricated by SU8 photolithography and (B) optical lenses are secured in place for integration of reagent vessels and hydraulic pumping fluid chambers. (C) Small disks next to lenses are fill pads while (D) larger pads next to microfluidic channels are bubble traps. **Bottom:** Real Time PCR Detection Microchip inclusive of (A) integrated electrodes for EHP pump actuation, (B) DNA purification, (C) PCR chamber, (D) magnetic separator and (E) bubble traps. The lab on-a-chip comes pre-loaded with reagents and can be quickly loaded into the supporting instrument.

Many groups have attempted to shrink down commercial flow cytometers by constructing them "on-chip" with microfluidics. Several microfabricated devices have been developed which flow beads or cells through an illuminating region for optical analysis. Typically, a microfluidic device is fabricated to guide the fluid stream through the illuminating region, and an optical detection system is coupled to the sample stream with free-space optical components carefully aligned to the flow-cell [21-23]. Waveguides were integrated into a micro-chip flow cytometer for guiding excitation illumination into the device [24], but to date fluorescence has been collected with an objective lens aligned to the flow-cell. The use of an objective lens to collect fluorescence requires calibration runs be made each time a fresh flow-cell is loaded so that the necessary optical alignment adjustments can be made by a skilled instrument operator.

FLOW CYTOMETER COMPONENTS

A typical flow cytometer contains an optical detection system aligned to a flow-cell. The optical system contains laser(s) which illuminate a small region of the flow-cell. The flow-cell functions to guide the sample to flow-through the focused portion of the illuminating beam. Photodetectors are positioned to detect the laser radiation which is scattered off the sample at specific angles. In addition, fluorescence is detected by rejecting the laser radiation and filtering for the desired wavelengths of the the optical spectrum.

SIGNAL PROCESSING

Based on the light scattering and emitted fluorescence, the various sub-populations present in the sample can be enumerated. When a sample is analyzed in a flow cytometer, the electrical signals recorded by the set of photodetectors contain unique characteristic patterns for the subpopulations of the sample. During a few minutes of data collection, flow cytometers acquire enormous amounts of data which are challenging to process. Recording the raw voltage traces from each of the photodetectors would require a prohibitively large amount of disk space, and performing digital signal processing on these recorded voltage traces would require a prohibitively long computation time. For this reason, the signals acquired by the photodetectors have historically been processed using analog circuits to measure basic characteristics of each photon-burst event in real-time. Instead of recording and analyzing digital voltage traces, the pulses at each detector are described by a few basic parameters and the set of pulses is compiled into a compact list of events for gating and analysis. Typically, a pulse amplifier and pulse integrator are used to describe the area under the pulse

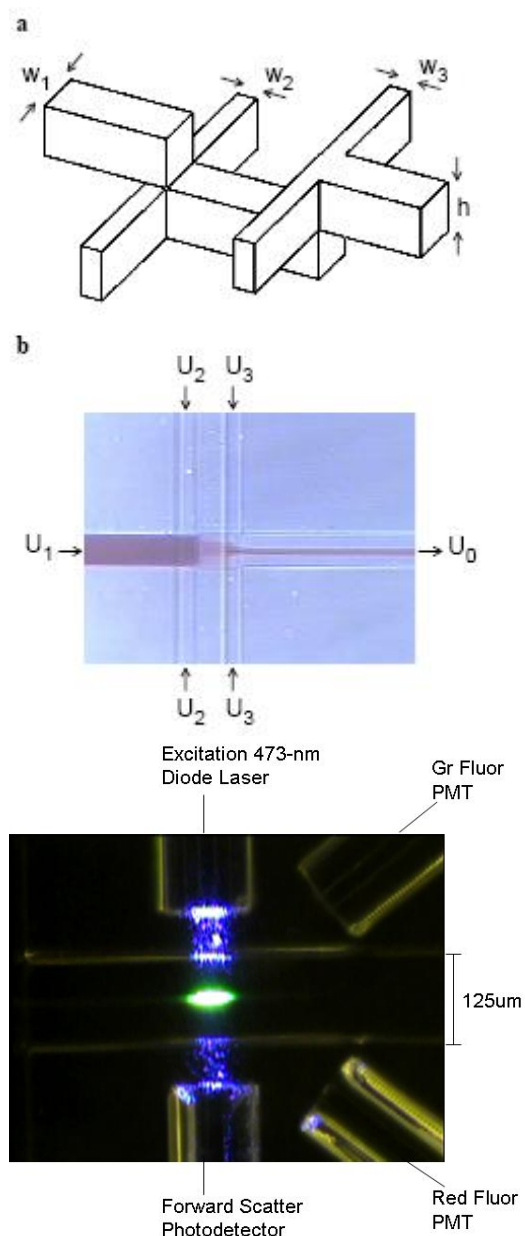


Figure 4 Flow Cytometer on-a-chip. **Top:** Schematic showing the design of the fluid focusing manifold. **Middle:** Optical micrograph of flow-cell under continuous-flow operation. The fluid under focusing is applied at volumetric rate U_1 ($\mu\text{L}/\text{min}$), and the focusing fluids are applied at rates U_2 and U_3 . **Bottom:** Optical micrograph showing a fluorescent bead pass through the illuminating beam of the microfabricated flow cytometer.

[25], time-to amplitude converters are used measure the width of the pulse, and peak detectors are used to measure the height of the pulse [26]. More recently, high speed digital signal processing technology has made it possible to process the signals digitally as they are acquired [27]. Today, plug-and-play data acquisition boards are available from National Instruments with analog-to-digital conversion (ADC) sampling rates as high as 60-MHz, and these have been used in proof-of-principle flow cytometer studies using LabView [28]. However, computer programs for the real-time digital processing of multiple data streams have yet to be written and will require considerable development. Therefore, either approach to signal processing, analog or digital, requires significant development effort before a fully functional flow cytometer can be realized. The most widely accepted method to signal processing appears to be a hybrid in which each photodetection channel contains some analog circuitry as needed as well as its own analog-to-digital converter. The parameters describing the pulse at each channel are cataloged by a central bus and lined up into a FIFO buffer for transmission to a computer [29].

ELECTRONIC GATING

The various species in a sample will scatter and fluoresce with characteristic patterns. Digital data analysis is performed on the parameterized list of photon bursts to organize the various events into “clusters of differentiation”. This step is referred to as gating. More advanced gating procedures are intimately tied to the data acquisition procedure through the user interface. Specifically, the instrument operator will observe a scatter-plot of, say, side scatter (SSC) versus forward scatter, in real-time, and select the cluster that corresponds to lymphocytes. Then, additional parameters can be viewed for the events present in the cluster in order to pick out subpopulations.

HYDRODYNAMIC FOCUSING

The ability to precisely control the position of a fluid stream vertically relative to the top and bottom walls of a microchannel is important for the development of portable integrated flow cytometer. This capability circumvents the mechanical adjustment steps normally required for aligning a lab-on-a-chip (LOC) with an optical detection system. This is particularly promising for the automation of optofluidic devices, which rely critically on optical alignment, for example in an integrated flow cytometer.

The first microfluidic hydrodynamic focusing devices focused a sample from two sides into a thin columnar stream [30]. Initial designs for focusing not only from the sides but also from above and below involved several fabrication steps with as many as five-layers of manifold housing (Sundararajan, 2004). Recent efforts have focused on fabrication simplicity. Previously, a three-dimensional focusing device was constructed from two patterned microfluidic layers [31]. This device functioned by overlapping the channels of one layer with the channels of the second layer junctions where the sample was impinged by fluid from the adjoining layer. Using three-stages of focusing, the sample was focused from above and below and from the sides, thereby maneuvering the sample into the center of the microchannel. Moreover, by adjusting the flow-rates of the various fluid inputs, the horizontal and vertical position of the focused stream could be controlled as shown by finite element simulations and brightfield microscopy. A device of similar design was subsequently characterized using confocal microscopy, and a cross-sectional image of the stream was obtained showing the sample focused to a dimension considerably smaller than the height of the microchannel [32]. Notably, a single-layer planar microfluidic device has also been used to focus a sample into the center of a microchannel [33]. However, controlling the vertical position of the sample does via straightforward adjustment to the relative flow-rates has not been achieved using this technique, which relies on a unique “microfluidic drifting” transport method.

Here, we describe a two-layer manifold following the same design concept as [32] but containing only two-stages of focusing instead of three-stages. This advance reduces the number of fluid inputs required to achieve three-dimensional focusing and simplifies device operation for use in a portable biosensor.

We used a combination of imaging and simulation to characterize the distribution of fluids in our device. A mixing experiment was performed in which the sample fluid contained fluorescein and the focusing fluid contained rhodamine. Images were obtained by pumping the fluids through the flow-cell under a confocal microscope. Subsequently, a series of image processing procedures was applied to the images revealing the concentration distributions of the fluorescent dyes. Using ANSYS computational fluid dynamics software, the presumptive concentration

distributions were computed for the flow-rates used during the experiment. With these two tools, imaging and simulation, we have investigated the effect of the focusing flow-rates on the vertical position of the focused sample. To our knowledge, this is the first study in microfluidic focusing to employ two-color confocal microscopy and to obtain a center-of-mass measurement for the position of the focused stream.

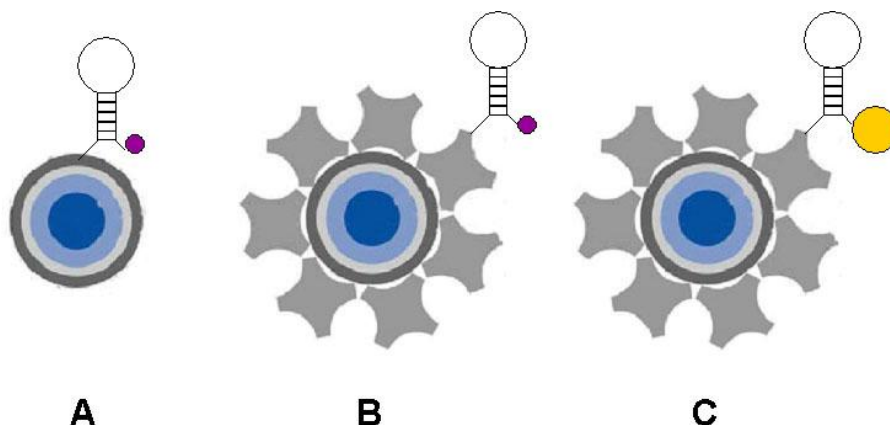


Figure 5 *Illustration showing three different quantum dot molecular beacon labeling strategies.* Carboxyl-modified quantum dots (blue core) were modified with amino-labeled molecular beacons (A) while streptavidin-modified quantum dots (blue core dot with surrounding gray streptavidin molecules) were modified with biotin-labeled molecular beacons. Both dabcyl and Iowa Black FQ quenchers (small purple circles) were used, as well as 1.4 nm Nanogold (gold colored circle).

INTEGRATED FLOW CYTOMETER

We have developed a microfabricated flow cytometer featuring integrated optics for purposes of both excitation and fluorescence detection (**Figure 4**). This advance in the optics yields a great ease-of-operation advantage over previous microfabricated flow cytometers. In particular, integrating optical fibers into the flow-cell relieves the instrument operator of optical alignment adjustment duties and enables twist-and-lock connection between the flow-cell and the supporting optics instrumentation. A fresh disposable flow-cell can be quickly loaded for each run, eliminating contamination issues between runs. Furthermore, since each flow-cell is identical in optical alignment, there is no need to perform mechanical position adjustments or run calibration beads with the loading of each flow-cell. The optics advance is made possible by a novel microfluidic fluid focusing manifold which guides the beads to pass through the illuminating beam of the flow cytometer.

ALLELE-SPECIFIC HYBRIDIZATION ASSAY

We have tested the integrated flow cytometer for its ability to distinguish between two sets of microspheres modified to contain single-stranded DNA (ssDNA) on the surface that differ by a single nucleotide. These microspheres were added to a heterogenous mixture of complementary DNA in which the two complementary sequences, which differed also by a single nucleotide from each other, contained spectrally independent

chromophores on the 5'-end. The assay used to distinguish between SNPs in this project is dependent on allele-specific oligonucleotide hybridization. The rationale behind it is that short oligonucleotides (15-20 nucleotides long) that contain the SNP in the middle of their sequence will hybridize to their complementary oligonucleotides but not to those that differ at the SNP site. For this study, a DNA sequence containing a SNP taken from the human GABRA2 gene was used. This particular SNP was chosen because it has been identified as having an average heterozygosity that is ideal for use in forensics [2]. GABRA2 is found in chromosome 4 at the 4p21 locus and encodes one of the major inhibitory neurotransmitters found in vertebrate brains [34].

1.4 QUANTUM DOT MOLECULAR BEACONS

Semiconductor quantum dots (QDs) have become attractive fluorophores for biosensing strategies [35, 36]. QDs are much brighter and more photostable than organic fluorophores, have narrow emission spectra (25-30nm full width at half maximum), and have broad absorption spectra. Because of the broad absorption spectra and large emission shift, QDs can be excited at wavelengths far-removed from their emission peak. Additionally, nearly all QDs of different emission peaks can be excited using a single, short-wavelength excitation source. There have been many recent reports of using QDs for biosensing applications, especially for multiplex detection strategies [37, 38].

Molecular beacons are comprised of a fluorophore and a quencher moiety attached to opposite ends of a single stranded DNA oligonucleotide. The sequence of the oligonucleotide is designed such that it preferentially base pairs with itself, forming a stem-loop structure. Included inside the loop region is a probe sequence that can bind to a complementary target DNA sequence. This hybridization event causes the stem-loop structure to open and spatially distance the fluorophore from the quencher. This decreases the FRET efficiency and results in increased emission from the fluorophore (donor).

The sensitivity of target detection is a function of the intensity of the signal and the background noise of the system. One method of increasing signal to noise ratios involves the use of fluorescence resonance energy transfer (FRET). FRET is a distance-dependent phenomenon that occurs when a donor fluorophore and an acceptor chromophore (quencher) are in close proximity [39]. When the fluorophore and quencher are within a certain distance from each other, excitation energy can be transferred from the fluorophore to the quencher, preventing fluorescence emission. The distance at which there is a 50% transfer in energy is known as the Förster Radius (R_o):

$$R_o = 9.78 \times 10^3 \left[k^2 \cdot n^2 \cdot Q_o \cdot J(\lambda) \right]^{1/6}$$

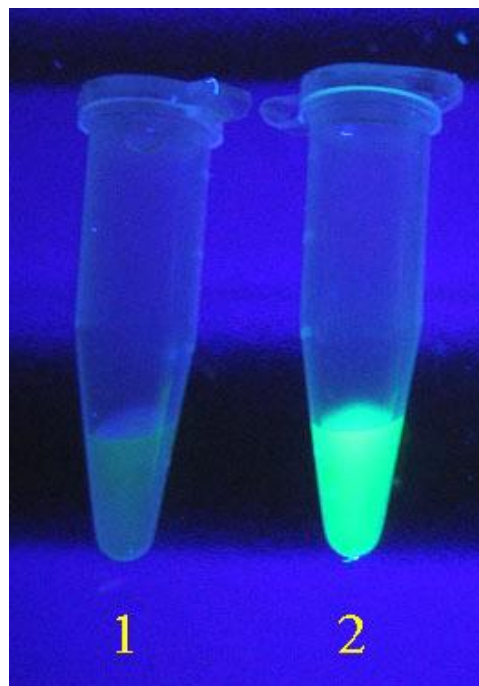


Figure 6. Image showing fluorescence quenching of quantum dots through the attachment of Iowa Black-modified molecular beacon. 1. Carb-IB quantum dot molecular beacons 2. Unmodified Qdot 525nm ITK quantum dots (right, Tube #2). Images were acquired with a Canon PowerShot A60 digital camera using a Labnet DyNA Light transilluminator as an excitation source. Abbreviated names are described in detail in Table 1

R_o is dependent upon (k) the orientation factor for dipole-dipole interactions, (n) the refractive index of the medium, (Q_o) the quantum efficiency of the donor, and ($J(\lambda)$) the spectral overlap integral between the donor and acceptor [40, 41]. Once R_o is known, the FRET efficiency (E) can be calculated for various distances (R) between the donor and the acceptor:

$$E = \frac{R_o^6}{R_o^6 + R^6}$$

Multiple detection techniques have been devised to harness this effect, including molecular beacons [10, 42-44].

Molecular beacons are extremely target-specific, primarily because of the competition between internal hybridization within the stem structure and hybridization between the target and the loop structure [42]. These dynamic interactions require specific hybridization between the target and loop structure to stabilize the molecular beacon in the open position. Additionally the stem and loop length of the molecular beacon can be altered to achieve either higher specificity and/or increased kinetic rate constants [45]. These features make molecular beacons attractive for biosensor detection applications.

To this end, we have developed several QD-based molecular beacons to be used for DNA-based detection strategies. Although the use of QDs as fluorescence donors in molecular beacons is not unprecedented [41], we present here a variety of methods for QD-molecular beacon synthesis, as well as a comparison of different fluorescent quenchers. Additionally, we demonstrate the effective use of QD-molecular beacons for DNA sequence detection.

1.5 LIGASE DETECTION REACTION WITH SURFACE ENHANCED RAMAN DETECTION

To increase the specificity of the RT-PCR format for more stringent SNP detection, a number of researchers have moved towards oligonucleotide ligation based methods such as the Ligase Detection Reaction (LDR) [46, 47]. In LDR, two primers anneal onto the DNA template at the site of a SNP. A discriminating base complimentary to the wild template (WT) or mutant (MT) allele is present at the 3' end of the upstream primer. A downstream primer common to both alleles is also present in the reaction. If the primers match the template perfectly, ligation occurs. Ligation will not occur if the primer and template are mismatched at the discriminating base. The ligation, which permanently links the two primers together, can be detected with a variety of different including FRET [48] and autoradiography [49].

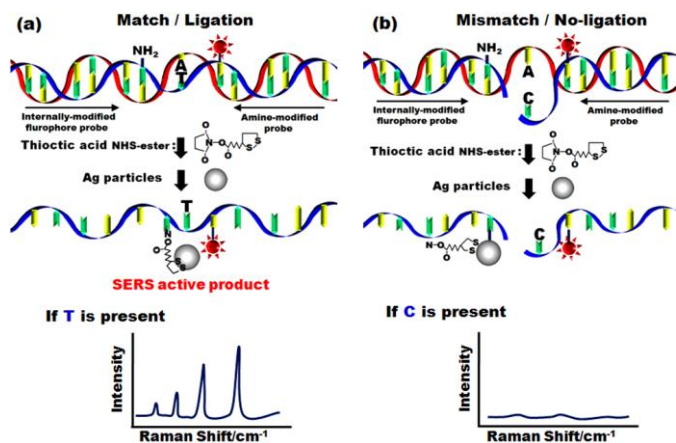


Figure 7 Overview of SERS Enhanced PCR/LDR detection reaction.

Most existing LDR and RT-PCR protocols use fluorescence tags as reporters and thus all have the same fundamental limitation in that spectral overlap between the reporter dyes limits the degree to which the reactions can be multiplexed. Typical fluorescent dyes have an emission spectrum with a full width-half maximum on the order of 50nm. Thus over the useful detection range of the spectrum (about 500nm to 750nm) one can at maximum expect to be able to discriminate on the order of 6 different dyes. This extends then to single tube reactions in that a maximum of 5 different SNPs can be screened for at once (1 color is used as an internal

calibration). To increase the number of molecular markers which can be screened for in a single step, one would like to develop a homogeneous detection system as simple as these but without the spectral overlap limitation.

One method by which this could be accomplished is through the use of a Surface Enhanced Raman Spectroscopy (SERS). A number of authors have developed SERS based techniques for sequence specific DNA detection. [50] for example demonstrated a three-component sandwich assay using Ag staining on Au seed particles to enhance SERS signals in DNA microarray format. In another example, [51] developed a peptide nucleic acid (PNA) based SERS DNA assay which enabled more rapid hybridization rates since the neutrally charged PNA weren't limited by the typical electrostatic repulsion between complementary DNA strands. A number of so called "molecular beacon" based SERS probe techniques have also been developed [52, 53]. These methods typically use a DNA hairpin structure with a Raman active molecule at one end and a metallic nanoparticle at the other which become separated following a hybridization thereby reducing the strength of the emitted SERS signal. [49] and [54] have also recently presented dye-coded DNA functionalized metal nanoparticles-based SERS methods which enabled greater sensitivity and repeatability in obtaining the SERS spectrum.

Here we present a new technique for SNPs detection that combines the selectivity and ease of use of the LDR reaction with the potential for large bandwidth and sensitivity of surfaced enhanced Raman spectroscopy (SERS). The LDR for discrimination of alleles is more accurate than the common hybridization reaction, provides high sensitivity and parallel analysis of several loci directly on genomic DNA in order to distinguish point mutations [55]. In this technique (illustrated in **Figure 1**) the upstream primer contains a SERS active dye and the discriminating 3' base, while the downstream primer contains an amine to which a silver nanoparticle (which acts as the SERS enhancer) is attached. When the two primers are ligated together (which occurs in the case of a perfect match with the template DNA) the dye is brought into close proximity to the nanoparticle and its Raman signature is detectable. In the case where ligation is not successful, the dye and nanoparticle remain separated and SERS enhancement will not occur.

We demonstrated the LDR-SERS detection reaction and apply it to the detection of point mutations in the K-ras oncogene. In collaboration with the Integrated Micro- and nano-fluidics Lab at Cornell, we implemented the reaction in a microfluidic chip containing electrokinetically active microwell devices [56] that enable us to enhance SERS detection by concentrating the reaction products from bulk phase into a confined volume for enhanced

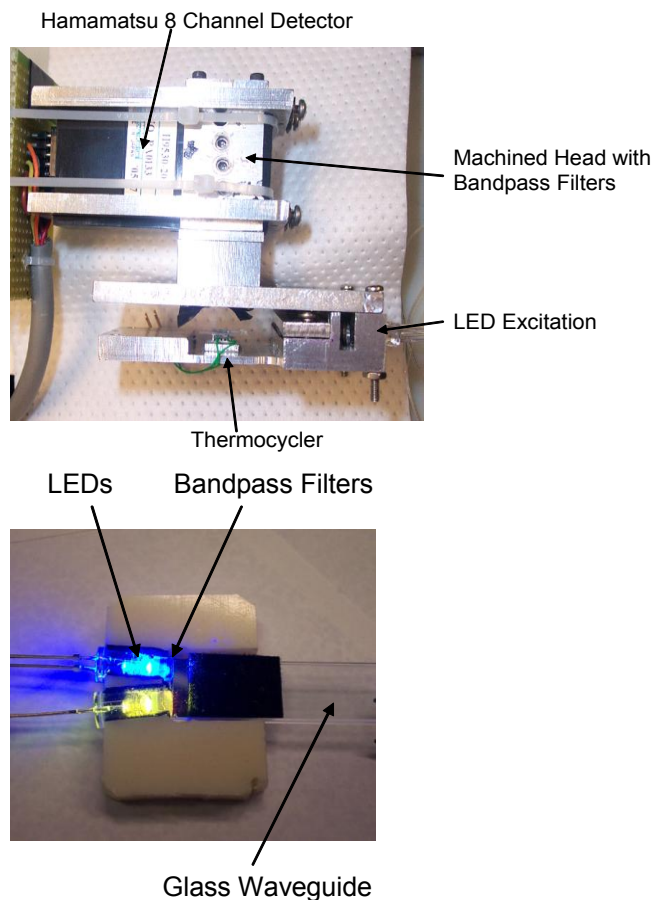


Figure 8 Multiplexed fluorescence detection instrumentation. A detection system capable of simultaneously detecting up to eight colors has been constructed and integrated into the microFLUIDICS DESKTOP. The system has undergone preliminary testing and is currently capable of simultaneously detecting fluorescence of four different wavelengths.

optical interrogation. In addition to SNP detection, we also demonstrated the quantitative nature of the reaction and characterize the limit of detection.

II. METHODS

2.1 PCR-BASED DETECTION MICROCHIP

MICROCHIP DESIGN AND FABRICATION

The sensor chip described here incorporates a microfabricated DNA purification chamber with a second PCR amplification chamber, connected by microfluidic channels. The DNA purification section contains an array of 10 μm square pillars that were etched 50 μm deep in silicon to form a microfluidic channel. Construction of the DNA purification region was performed as previously described [12]. The PCR amplification chamber was constructed using soft lithography techniques for poly(dimethyl siloxane) (PDMS) and SU-8 photoresist (Microchem, Newton, MA) described by [57]. Briefly, PDMS was cured in an SU-8 mold of the PCR chamber and then bonded to a 50 μm thick PDMS membrane. Bonding was achieved by exposing both PDMS substrates to an oxygen plasma for 20 sec in a Harrick Model PDC-001 (Ossining, NY) Plasma Cleaner/Sterilizer at 200-600 mTorr with 30W DC power applied to the RF coil. The PDMS substrates were then pressed together and baked at 60 $^{\circ}\text{C}$ for 30 min to achieve maximum bonding strength. After bonding, the PDMS structures were peeled from the wafer and were bonded to the microfabricated Si chips to seal the chambers. For fluidic connections 30ga stainless steel tubing was inserted into holes in the PDMS and was glued in place using Miller-Stephenson 907 Epoxy (Danbury, CT). Connections between the tubing and the syringe pump were made using 0.010" microbore tubing (Small Parts, Miami Lakes, FL). An assembled microchip is shown in **Figure 1**. Microfabrication of this device was carried out at the Cornell Nanoscale Facility (Ithaca, NY).

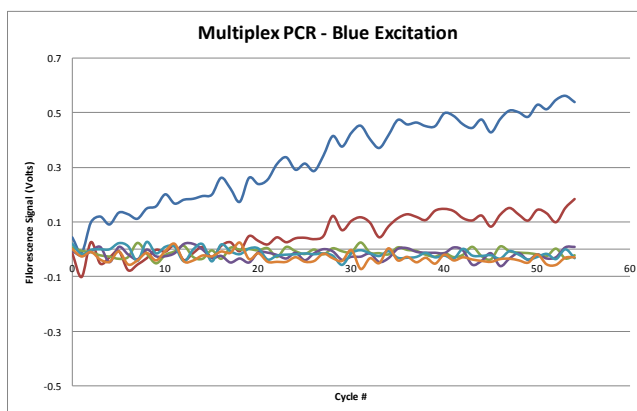
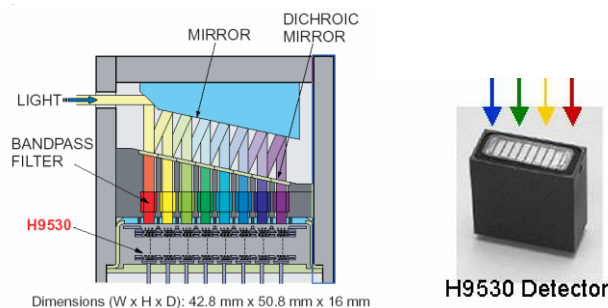


Figure 9 Multiplexed RT-PCR Optical Detection System. The detection system is designed to simultaneously detect multiple fluorescent dyes in a single PCR assay. Integral to the system is a multicolor PMT detector H9530 from Hamamatsu.

We have developed a SYBR Green real-time PCR assay for SNP detection (see prior report). Under the guidance of the NYSP Forensic Investigation Center, we are examining additionally SNP targets.

PCR AMPLIFICATION

PCR reactions consisted of 25 μl SYBR Green JumpStart Taq Ready Mix (Sigma, St. Louis, MO), 50 nmol of each primer, 1 μl template DNA, in a total volume of 50 μl . Reactions were cycled in an MJ Research thermocycler (Waltham, MA) under the following conditions: 95 $^{\circ}\text{C}$ denaturation for 5 min, 40 cycles of 95 $^{\circ}\text{C}$ for 10 seconds,

57°C for 15 seconds, 72°C for 20 seconds, followed by a 5 min extension at 72°C. DNA amplification was confirmed by gel electrophoresis. Real-time PCR was performed on an ABI Prism 7000 real-time thermocycler (Applied Biosystems, Foster City, CA). For these experiments, various amounts of template DNA were used in the same reaction conditions as described above. Microchip-based PCR amplification was performed using the same reaction conditions and fluorescence was monitored during the 72°C extension step of each cycle. For optimized microchip PCR, SYBR Green JumpStart Ready Mix was mixed at 1.35 times the standard concentration for a 50µl reaction: 25µl Ready Mix, 50nmol each primer, 2.5 units Stratagene Sure Start Taq polymerase (La Jolla,CA), and dH₂O to a final volume of 37.5µl.

MICROFLUIDICS DESKTOP

A microcontroller-based instrument was built to automate fluid handling and control thermal cycling operation. The system was designed to require low power (20W) and occupy a small footprint for future development of a portable, point-of-care device **Figure 1**. The instrument has an electronics module consisting of a controller board and power amplifiers for driving an automatic syringe pump, a thermoelectric heater/cooler, a fluorescence excitation/emission module, and a pressure valve. During operation, the entire system is controlled by a Z-world microcontroller board (Rabbit, Davis, CA) and is programmed to carry out the amplification steps sequentially. In order to provide accurate fluid control and movement throughout the system, a multiple-channel syringe pump was designed to allow for parallel pumping of multiple fluids. A single Faulhaber AM1525-15A 102:1 HEAM152412 stepper motor (MicroMo, Clearwater, FL) actuates this pump that can drive individual syringes by selective engagement using PIC Design, Inc. RW1-333 electromagnetic clutches (Middlebury, CT). Fluid flow direction and chip pressurization are controlled by a Moog MicroValve (East Aurora, NY).



Figure 10. EHP pumps integrated into a complete testing system. Small disks next to lenses are fill pads while larger pads next to microfluidic channels are bubble traps.

The temperature of the detection microchip is cycled by a Melcor HOT 2.1-31-F2A (Trenton, NJ) thermoelectric heater/cooler (TEC) that is, in turn, controlled by a Hytek (Carson City, NV) 5640 TEC control chip and Hytek 5670 control board. A 10kΩ thermistor mounted on the chip measures the temperature and is used as the feedback element by the microcontroller to control cycling parameters. The Hytek 5670 control board was modified so that three separate temperature set-points could be achieved by switching between temperature set-point resistors with relay switches.

Optical detection for real-time PCR was achieved using an LED-based fluorescence excitation source and miniaturized photomultiplier tube (PMT) for detection. The fluorescence detection system both excites and detects fluorescence in PCR microchips during amplification reactions and is similar to a system described previously [58]. The sample is excited by a 480nm blue light emitting diode (LED) requiring 80mW of power. The LED is filtered using a Chroma Inc. D480/30x excitation filter and laterally excites the detection microchip through a chrome-coated glass waveguide. The resulting fluorescence is filtered by two Chroma Inc. (Rockingham, VT) D535/40m emission filters and detected by a Hamamatsu (Bridgewater, NJ) H5784-20 photomultiplier tube (PMT) at 520nm. The light from the LED uniformly illuminates the detection region on the chip while the PMT detects the fluorescent emission. Plano-convex lenses were used to focus emitted light from the detection microchip through the first emission filter, off of a 45° mirror, through a second emission filter and into the PMT. The following specifications describe the optical parameters of the system. The clear aperture for imaging the reaction chamber is 6.46 mm in diameter which is 33% of the area of the 10 mm square chamber. This translates into a 6.46mm spot size at the focal point. The numerical aperture (of the objective lens) is 0.41 and has a working F-

number of 0.925. Using Equation 1 (below), the depth of focus (DOF) for the microfluidic channels was calculated to 574 μ m (where A is the F-number, so is the object distance, f is the focal length, and d is the image size). The microfluidic channels of the PCR chamber are 100 μ m in height, well within the depth of focus. The image size on the PMT is 4.92 mm in diameter and the image NA is 0.54. The magnification for the system is 0.75X.

$$DOF = \frac{2Ads_o(s_o - f)f^2}{f^4 - A^2d^2s_o^2} \quad (1)$$

The entire system is mounted in a portable box enclosure (**Figure 1**) that measures (36cm x 28cm x 15cm) and has a total weight of 4 kg. During a typical detection protocol, a program is loaded into the Z-world controller's flash memory from a laptop computer through serial inputs. The program executes fluid pumping, chip pressurization, thermal cycling, and fluorescence detection sequentially. During the real-time PCR reaction, fluorescence data is collected during the 72°C extension step and is either stored in the microcontroller's flash memory or is directly output to a laptop computer.

MICROFLUIDICS DESKTOP MULTIPLEX

The H9530 is mounted on a machined filter head which has the optical bandpass filters arranged inside. The filters are positioned on small screws which allow angular adjustment for optimization. The detection module is mounted on the platform which includes the PCR thermocycler and LED excitation in precise alignment. The design of the detection module is compatible with the current microFLUIDICS Desktop instrument and can be interchanged rapidly with the single color system.

The initial demonstration of our microFLUIDICS Desktop MULTIPLEX is accomplished using the following criteria for design of the optical filters and choice of individual fluorescent dyes: For excitation, we use two LEDs for excitation of the four dyes (**Figure 8**). The 480nm LED excites the FITC and JOE dyes while the 580 nm LED excites the ROX, CY5, CY5.5 and CY7 dyes. The two LEDs are bandpass filtered and coupled

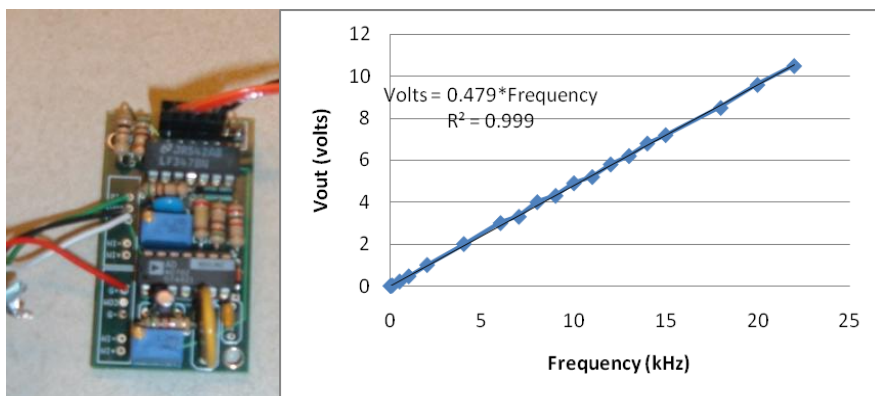


Figure 11. The AD650 Frequency to Voltage converter used to drive EHP pump is shown with a plot of the voltage output vs. the applied frequency.

into a glass waveguide, which is then coupled into the side of the PCR-based detection microchip. Dichroic band pass filters make it possible to provide four distinct excitation wavelengths to the PCR amplification chamber. The band-pass filters select the proper wavelength for each of the fluorescent dyes to be analyzed. Detection of human SNPs with PCR-based melting curve analysis

MELTING CURVE ANALYSIS

Groups have shown that single-tube amplification and detection of polymorphic alleles using PCR-based melting curves is possible if the melting temperatures of the two alleles are sufficiently different [1]. This technique was later extended by other groups to SNP genotyping by introducing a 10-bp GC clamp onto the 5' end of one of the two allele-specific primers, thereby introducing a difference in melting temperature between the two allelic PCR

products [2]. We explored the prospect of implementing this technique for SNP detection in a portable instrument. We extracted human DNA using an extraction procedure which is compatible with our micro-chip based technique for DNA extraction, and we subsequently acquired melting curves on this sample for the two different alleles of ABCA1 R219K. The K-variant of this relatively common SNP is reportedly associated with increased levels of high-density lipoprotein (HDL) and reduced coronary artery disease [3].

Primers were obtained from IDTDNA. The sequences for the ABCA1-K-allele-FWD primer and the ABCA1-R-allele-FWD primer were 5'-CTGAGCTTTGTGGCCTACCTAA-3' and 5'-CGCGCCGGCCGCGGGACTTTGTGGCCTACCcAG-3', where the GC-clamp, which raises the melting temperature of the R-allele, has been underlined. The sequence for the ABCA1-REV primer was 5'-GGATGTCCATGTTGGAACGAA-3'. These are the same sequences pointed out previously by [2]. DNA was extracted from a human sample using the ethanol extraction technique previously described [4]. The amplification micromix contained 100-uL of Sigma SYBR, 8-uL of 10-uM ABCA1-R-allele-FWD primer, 8-uL of 10-uM ABCA1-R-allele-REV primer, 4-uL extracted human DNA, 74-uL dH2O, and 1-uL Sure Strand Taq. Melting curves were acquired using an ABI-7000 Sequence Detection System. The thermocycler was set at 95C for 5-min followed by 45 cycles of 95C for 15-sec followed by 60C for 60-sec.

2.2 ELECTROLYTIC HYDRAULIC MICROPUMP

PUMP DESIGN

To improve upon the original EHP we redesigned the fluid chambers to 1) make the pumping more consistent, and 2) to remove as much dead volume as possible. The dead volume translated into a disconnect between the actuation of the system and the fluid output. The original design used Teflon disks as molds to form the pump chambers (in the soft silicone polymer PDMS). The cylindrical chambers created dead volume in the pumps where bubbles became trapped and where the flexible membrane layer could not exert force. The chambers were therefore modified from cylindrical to hemispherical, creating a dome-shaped chamber. Bubbles formed in the electrolyte chamber uniformly rose to the peak of this dome and the flexible membrane could be stretched to make contact with the entire chamber surface. This reduced all of the dead volume in the chambers and resulted in more consistent pumping profiles.

ELECTRODE DESIGN

Preliminary electrodes that consisted of gold evaporated on glass tended to peel away from the glass when voltage was applied to the electrolyte solutions. The electrolyte system is TRIS-acetate, EDTA. To immediately compensate for challenges in the use of evaporated gold electrodes, we moved to a different electrode configuration. The initial attempt to improve the electrodes utilized stainless steel mesh. Steel mesh with a grid size of 0.2mm was inserted into the electrolysis chamber and used to drive the system. Unfortunately, it was difficult to create a strong bond between PDMS and stainless steel, so during pressure testing, the chamber leaked. As an alternative we utilized stainless steel electrodes that could be secured into the pumping chambers. Polystyrene was used as the base material for all of the pumps that were characterized during this effort. We used stainless steel pins (Swan Secure Products, Inc, Baltimore, MD) and secured the pins in the polystyrene base of the electrolyte pump chambers. These electrodes showed no signs of degradation over a five week period and the completed system could withstand 150 kPa of pressure without

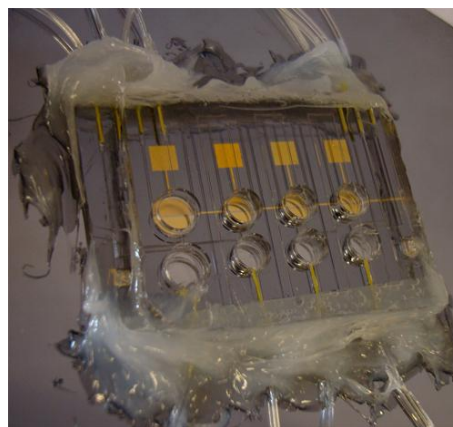


Figure 12 Assembled and sealed gold-electrode electrolytic hydraulic micropump device consisting of four separate EHPs

leaking. While these stainless steel electrodes represented an option for the testing as described below, the integration of the electrodes represented a challenge in developing a more integrated manufacturing approach to the system.

PUMP FILLING AND FLUID CONNECTIONS

To further optimize the EHP design, we also sought to develop a method to fill the EHP chambers, and to develop novel microfluidic connections between EHPs and microfluidic components. A possible filling solution is to include filling pads for each pump layer into the EHP design (**Figure 10**). Our previous method was to insert hypodermic needles into the main chambers to add the reagents, but this method was time consuming and unreliable. With the integrated pads, filling the chambers was easier and there was a reduced chance of mistakenly piercing the membrane.

We designed microfluidic connectors to connect the EHP pumps to exterior fluidic components. To accomplish this we converted SMA fiber optic connectors for use with microfluidic applications. One side of the connector is made of a SMA fiber optic connector where 0.25mm 27 gauge stainless steel tubing is attached, while the corresponding side incorporates 0.62mm Tygon tubing. Small gauge tubing from microfluidic components (Tygon, PEEK, etc.) is then attached to these using pressure-tight fittings. The SMA mating adapter keeps these two pieces aligned, and when tightened, forms a watertight seal between the two connectors. During testing, the seal withstood pressures of at least 150 kPa, which is more than adequate for most microfluidic applications. The connection is reusable and can be used repeatedly without compromising its watertight seal.

ELECTRONIC FLUID CONTROL SYSTEM

To provide fluid flow rate control, we developed an electronic control board that could actively modulate the applied voltage that initiated electrolysis. Calibration curves were created for frequency vs. voltage, and precise flow rates could be delivered by setting the output frequency and voltage of the electronic control board (**Figure 11**). We utilized an AD650 (Analog Devices, Inc) frequency to voltage converter and a prototype circuit board was designed and completed. The device was designed to work with power from batteries or with a transformer and maximum voltage output was increased to 10.6VDC through addition of an operational amplifier. This circuit was used to drive EHPs with a National Instruments USB-6009 data acquisition system using LabVIEW (National Instruments, Austin, TX) software. This system was used to operate the pumps during flow calibration tests. While this controller provided some measure of regulation on the pumping rates, the lack of any feed-back control limited the overall precision of the EHP units.

GOLD ELECTRODES

In order to further miniaturize the system, 250 nm-thick gold electrodes were e-beam evaporated onto a bare silicon wafer and annealed at 400°C for 120 minutes. The annealing step prevents the rapid peeling of gold during electrolysis and essentially doubles the life of the device. The PDMS chamber assembly is plasma treated, aligned to the gold electrodes, and bonded to the silicon surface. Small gauge tubing (PEEK) was inserted into the inlets and outlets, and secured using silicone sealant. Copper wires were attached to the electrode pads using conductive silver epoxy, and hooked up to voltage source. Our initial experiments with gold electrodes resulted in fast degradation of the electrodes. Switching from DC operation to AC operation, in conjunction with the gold annealing step, allowed the electrodes to remain intact and fully functional for up to 40 minutes, which is sufficient time for the EHPs to serve their purpose of pumping the small-volume fluids. The assembled device is shown in **Figure 12**.

2.3 INTEGRATED FLOW CYTOMETER

FABRICATION

The flow-cell was fabricated by bonding together two patterned pieces of PDMS using a contact-aligner. Briefly, two polydimethylsiloxane (PDMS) masters were fabricated by patterning polyimide resist onto silicon wafers with photolithography. A thickness of resist of 125- μm was obtained by applying two rounds of spin-coating of SU8-75 (Microchem Corporation, USA) at 2375-RPMs for 40-seconds for each silicon wafer. Each round of spin-coating was followed by 20-minutes baking at 95-C on a hotplate. After cooling, the coated wafer was exposed to ultraviolet light through a patterned chrome mask and then post-exposure baked for 12-minutes at 95-C. The wafers were chemically developed to remove resist from all unexposed locations and then rinsed with water followed by Isopropyl Alcohol. After rinsing, PDMS was spun onto the masters at 250-RPMs for 60-seconds in order to obtain molds of uniform thickness for the subsequent contact alignment procedure. The PDMS was then cured by baking at 70°C for 45-Minutes.

The critical step in the fabrication of this flow-cell was the alignment of the two pieces of PDMS relative to one another as they were brought into contact. Immediately preceding alignment, the two pieces were peeled from their masters and exposed to a 200-Watts oxygen plasma, patterned side up, for 20-seconds. Next, the pieces were placed into aligned contact using a contact aligner (III-HR, Hybrid Technology Group, USA) and subsequently baked for 30-minutes at 70°C to achieve permanent bonding. The flow-cells were packaged by connecting tubing lines (Tygon Tubing PVC .020", Small Parts, Inc.) to the input of each fluid channel via 27-gauge stainless steel tubing (Small Parts, Inc.).

SIMULATIONS

Analysis of two-species transport was performed using commercially available finite element-based software. The flow-cell geometry was defined in ANSYS Multiphysics 10.0 as a 3D FLOTRAN-142 element and meshed with an element edge length of 5- μm . A load of Species 1, molecular weight 480-g/mol in water, corresponding to fluorescein, was applied to the central input, and a load of Species 2, molecular weight 330-g/mol in water, corresponding to rhodamine, was applied to the focusing inputs. A mass diffusion coefficient of $5\text{e-}6\mu\text{m}^2/\text{s}$ was assumed for both species. A steady-state solution was obtained by solving, together, the Navier-stokes equation and the convection-diffusion equation using 60-global iterations of the ANSYS precondjugated residual method solver. From this solution, a contour plot was obtained of the concentration distribution of fluorescein over the volume of the manifold. The color-map was defined in ANSYS such that the range of normalized values of concentration, [0, 1], mapped linearly to the range of pixel values [0, 255]. One contour plot was obtained for the concentration of fluorescein and another contour plot was obtained for the concentration of rhodamine. The two contour plots were exported as TIF files and then, using ImageJ Image Processing Software, were overlaid onto the same image. Cross-sectional images were obtained by altering the viewpoint in ANSYS from 3-D view to cross-sectional view and then repeating the export and overlay procedure.

CONFOCAL MICROSCOPY

Experimental images of the distributions of fluids were obtained using an inverted laser-scanning spectral confocal microscope (LSM 510-META, Zeiss, Inc.). The microscope is fitted with two excitation sources: a 30-mW

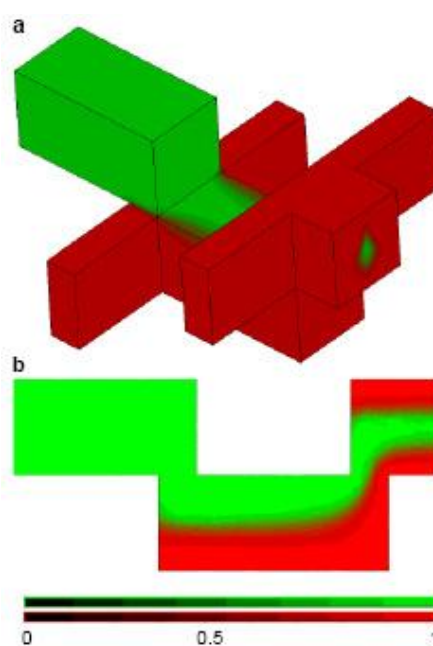


Figure 13 ANSYS simulations of two-species mixing. Concentration distributions are shown where the sample fluid contained fluorescein and the focusing fluids contained rhodamine. **a** three-dimensional view; **b** cross-sectional view taken vertically through the center of the main channel along the direction of flow

Argon Laser (471-nm, 488-nm) and a 15-mW diode-pumped solid-state laser (561-nm). The microscope acquires spectral image data by using a grating to disperse the signal onto a multidetector array. One detector was filtered to detect fluorescence from the fluorescein-labeled fluids in the range of 505-555-nm, and the other detector was filtered to detect fluorescence from the rhodamine-labeled fluids in the range of 575-650-nm. Line-wise multi-tracking was used to further reduce spectral cross-talk by eliminating the simultaneous emission of both chromophores by both excitation sources. Multi-tracking refers to the electronic control of the scanners and laser lines to switch the excitation wavelength between line-scans [59]. Moreover, the 471-nm line of the Argon laser was used for excitation of the fluorescein because the shorter-wavelength mode of excitation reduced the spectral bleedthrough of fluorescence from rhodamine into the green-channel PMT compared to the 488-nm line.

The flow-cell was mounted on the sample holder of the microscope and syringe pumps were placed in proximity (PHD 2000, Harvard Instruments). The sample contained 0.2-mM fluorescein in Tris Buffer pH 8.0, and the sheath fluid contained 0.2-mM Rhodamine 6G in water. Particulates were eliminated from both solutions prior to the experiment using 0.45- μm syringe filters (21053-25, Corning, USA). The flow-cell was operated under continuous-flow conditions at Reynold's number $R=2.7$ for the duration of the experiment. Between the adjustment to the flow-rates and the acquisition of an experimental image, five minutes was allowed to pass to ensure that each image represents the steady-state distribution. On a few occasions, instabilities arose when an air bubble entered the microchannel. When this occurred, we waited for the bubble to pass and then recorded an image after the fluids had returned to their steady-state distribution.

Images were scanned through a cross-section of the channel using a 20X microscope objective. The distance between the depth of successive scan-lines was 1.0-micron, and the total depth of the yz-scan was typically 160- μm . The horizontal scan-resolution was 0.29- μm , and the width of the scan was 148- μm . Therefore, a raw yz-scan typically contained 512x160 rectangular pixels. These data were extrapolated by the Zeiss LSM Imaging Software accompanying the microscope to deliver images containing square-pixels, with each pixel representing an area of 0.29- μm x 0.29- μm . The resulting two-color images typically contained 512x554-pixels, and these were exported as TIF files for subsequent processing and analysis.

IMAGE ANALYSIS

Images were imported into MATLAB for processing (**Figure 14**). Each pixel contained values for red, green, and blue, and the blue pixel-values were all zero. Therefore, each image could be thought of as an overlay of one green image and one red image onto the same grid of pixels, where the red image contained intensity values detected by the red-channel PMT, $I_R(x,y)$, and the green image contained the intensity values detected by the green-channel PMT $I_G(x,y)$. Therefore, each pixel contained red-values I_R and green-values I_G each in the range of 0 to 255.

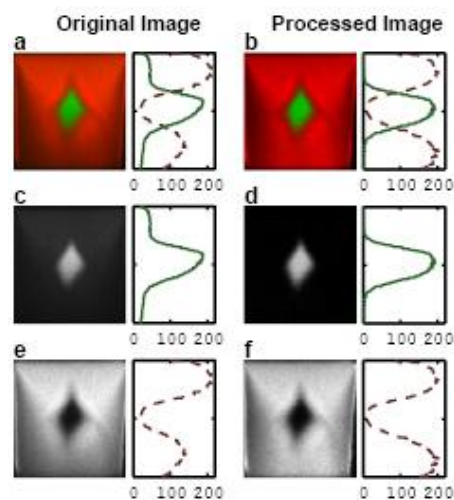


Figure 14 *Fluorescence micrographs and intensity profiles showing the effect of image processing.* **a** Original image alongside a profile of the green-pixel-values (solid line) and red-pixel-values (dashed line) obtained along the vertical center of the image; **b** processed image; **c** original image, pixel green-values; **d** processed image, pixel green-values; **e** original image, pixel red-values; **f** processed image, pixel red-values.

Our image registration fits the walls of the microchannel with a rectangle by first segmenting the image and then fitting the segmented image with horizontal and vertical lines. Segmentation was achieved with the Sobel Operator using the edge() function in MATLAB. Next, a horizontal line was fit to the top edge by minimizing the sum of the squares of differences between the pixels of the detected top edge and the horizontal line. The bottom edge and the left and right edges were then obtained in the same manner. The error associated with locating the height of the bottom and top channel walls was estimated by calculating the standard deviation of the Sobel-detected pixels about each fitted walls; specifically,

$$\sigma = \sqrt{\frac{1}{N} \sum_{i=1}^N (y_i - y_{FIT})^2}$$

Spectral unmixing was performed. Briefly, a specific fraction of the red-pixel-values were subtracted from the green pixel-values of the images. This fraction was calculated from the flat-field image in which all of the fluids were loaded with rhodamine, as explained in detail in Appendix 1.

Depth-dependence compensation was performed according to a linear mathematical correction method. Briefly, the brightness of the image was observed to decay with depth. The slope of decay of brightness was measured separately for the red-pixel-values and the green-pixel-values by analyzing field images in which the microchannel contained only rhodamine or only fluorescein, respectively. Based on these calculations, the depth-decay was removed from the experimental images using a linear transformation.

The image analysis program calculates the center of mass of the fluorescein-labeled fluid according to the usual formula:

$$y_{CM} = \frac{\sum_{i,j} y_j \cdot I'_G(x_i, y_j)}{\sum_{i,j} I'_G(x_i, y_j)}$$

where x_i and y_i refer to pixels measured relative to the best-fit horizontal and vertical walls of the microchannel and I'_G refers to the green pixel-values of the image post-processing. The calculation was implemented in matlab using a for loop.

INTEGRATED FLOW CYTOMETER

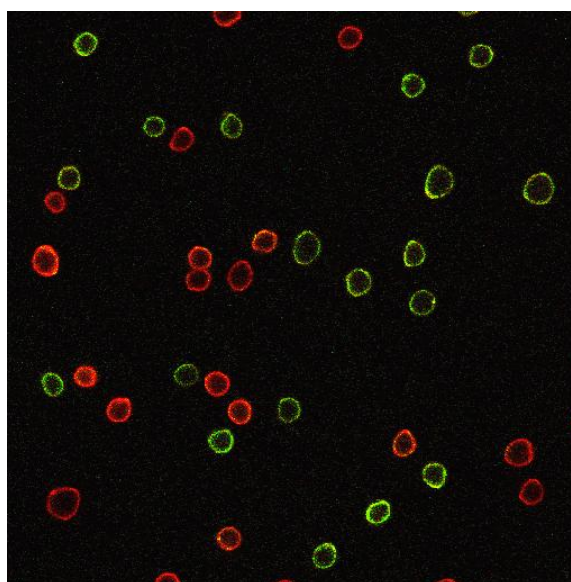
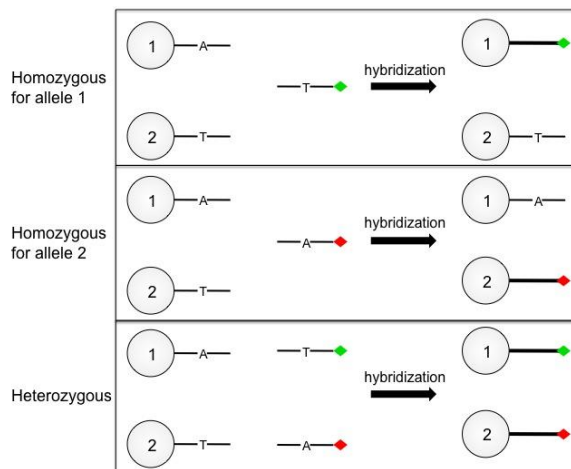


Figure 15 Allele-specific hybridization assay. **Top:** Diagram depicting the hybridization assay of labeled DNA to beads surface-modified to contain ssDNA. **Bottom:** Confocal microscopy image showing the hybridization specificity of a heterogeneous mix of two flavors of beads mixed with a heterogeneous mix of two flavors of labeled DNA, in which the two flavors differ by one nucleotide.

The device was fabricated by a replica-molding process known as soft lithography (Xia, 1998), which allows multiple identical flow-cells to be inexpensively fabricated. Briefly, a negative master mold is created by patterning SU-8 polyimide resist (Microchem) on a silicon wafer with photolithography. The resist viscosity and spinner speed were chosen such that the mold feature height was 125- μm after patterning, which corresponds to the diameter of an optical fiber. Silicone elastomer was poured onto the SU-8-on-silicon masters and cured for 2-hours at 60-C. One piece was peeled from each of two masters and exposed to a 200-W oxygen plasma for 40-seconds. Next, the two pieces were brought into aligned contact under a contact aligner and subsequently baked for 20-minutes at 60-C to encourage permanent adhesion. Fluid tubing lines (Tygon Tubing PVC .020", Small Parts, Inc.) were connected to the fluid channels via 27-gauge steel tubing and the connections were sealed with epoxy.

The flow-cell layout included two components: the fluid focusing manifold and the optical detection system. The feature height of both components was chosen to be 125- μm . Several fluid channels were defined on layouts for two wafers because the fluid focusing occurs at the interface between two patterned surfaces. Optical fiber insertion guides were included in the flow-cell layout that defined the output of the manifold and therefore the optical excitation region. In this manner, alignment of the optical fibers with interrogation is ensured within lithographic precision. After flow-cell fabrication, optical fibers were sheath-stripped and cleaved and then inserted into the fiber insertion guides. Optical adhesive was inserted into the fiber insertion guide during this process using a syringe and subsequently cured with ultraviolet radiation.

An argon ion laser was used as an excitation source and was coupled into the excitation fiber. After selecting for the 488-nm line and then coupling into the fiber, the excitation power guided into the flow-cell was approximately 1-mW. Multiple detection fibers were integrated into the flow-cell and were connected to photomultiplier tubes (Hamamatsu, Japan). Single-mode fibers were used to guide excitation illumination into the flow-cell while multimode fibers were used to collect fluorescence from the excitation region (ThorLabs). A collimation tube containing optical filters was placed at the entrance of each photodetector and was fitted with an optical fiber collimation adapter for twist-and-lock connection with the flow-cell. Each photodetector and filter tube combination were placed in a machined aluminum housing, which maintained alignment of the collected light into the photodetector and shielded the detector from ambient light. Three photomultiplier tubes (H5784, Hamamatsu) were coupled to the flow-cell in this fashion and each were connected to a 4-channel data-acquisition port (USB-6009, National Instruments). Voltage-traces were acquired at 10-kHz using a Labview program and

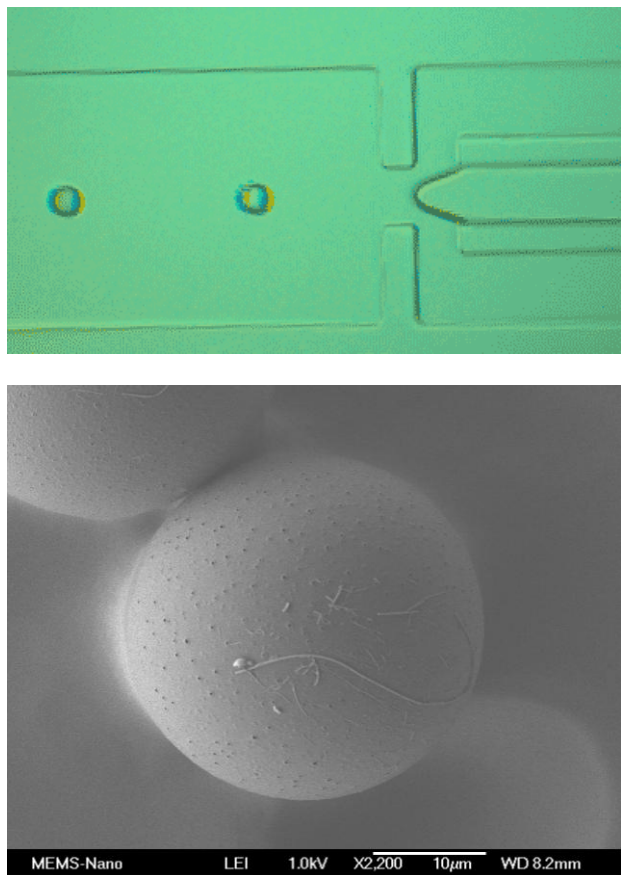


Figure 16 Microfluidic assembly of microparticles for flow cytometry. **Top:** Optical micrograph showing a water-in-oil reverse-phase emulsion. **Bottom:** Scanning Electron Micrograph showing polymer microspheres synthesized using the microfluidic flow-cell. Here, the water phase was loaded with polymer and the flow-cell outlet was directed into a solution of ethanol. The polymer, poly-vinyl(pyridine), is insoluble in ethanol and forms hard microspheres upon collection from the flow-cell.

saved as ASCII text files on a personal computer. The PMTs were powered and controlled using electronic power supplies constructed in-house which deliver a steady voltage source by means of a DC-DC converter (DKE10A-15, Mean-well, USA) and which allow the control voltage (gain) to be tuned between 0V and 1V using a resistive voltage divider. For purposes of repeatability, the gain to each PMT was coupled to a panel LED voltage monitor (DMS-20LCD-1-5-C, Murata Power Solutions). For microspheres in the range of 3 μ m-5 μ m, the PMTs used for scattered light were set at 0.525V, whereas the PMTs for red and green fluorescence were set at 0.8V.

The voltage traces were analyzed using matlab post run-time. The analysis program could be set to trigger off of the forward scatter (FSC), side-scatter (SSC), or green fluorescence (GFP) channels. A photon burst was triggered as an event if the voltage rose to a height of more than 4-standard deviations above the mean. The running average and standard deviation were calculated using an integration time of 250-ms. In order to obtain scatter-plots (e.g., **Figure 18**), the peak voltage value less the base-line voltage value was obtained for each photon burst event.

As an experiment, a 0.1%-solids solution of 2- μ m polymer microspheres in bead suspension solution (.05M NaH₂PO₄ 0.1% NaCl pH 7.8, 0.2% gelatin added, syringe filtered) were added to the sample input of the microfabricated flow cytometer. Then, the ratio of the top focusing fluid to the bottom focusing fluid was swept over a range of several orders of magnitude, analogous to the experiment performed while characterizing the manifold. This shifted the bead stream up and down. The bead stream was first positioned near the top of the microchannel and then translated down in steps. At each step, data was acquired for 5-minutes at rates of up to 100-events per second. These data were analyzed post-data acquisition by scattering off the FSC, SSC, and GFP signals. The number of events triggered off of each channel was obtained for each set of flow-rates.

ALLELE-SPECIFIC SNP HYBRIDIZATION ASSAY

We have developed a protocol for covalent attachment of probe DNA to the surface of optically barcoded beads. This is achieved by EDC chemistry of a 5' amine-terminated single-stranded DNA to the carboxylated surface of a polystyrene microsphere. We subsequently hybridized complementary sequences to these bead probes and these complementary sequences were fluorescently labeled with an Oregon Green Chromophore.

For hybridization, 25 μ L of microspheres respectively bound to allele 1 and allele 2 probes were combined, centrifuged and resuspended in 25 μ L of hybridization buffer (0.1M Tris buffer, pH 8.0, 2mM MgCl₂). 4 μ L of 25 μ M target DNA was added to the resuspended microspheres. Three such assays were set up, the first with 4 μ L of allele 1 target DNA, the second with 4 μ L of allele 2 target DNA, and the third with 2 μ L of allele 1 target DNA and 2 μ L of allele 2 target DNA; the assays thus simulated DNA samples from targets that were homozygous for allele 1,

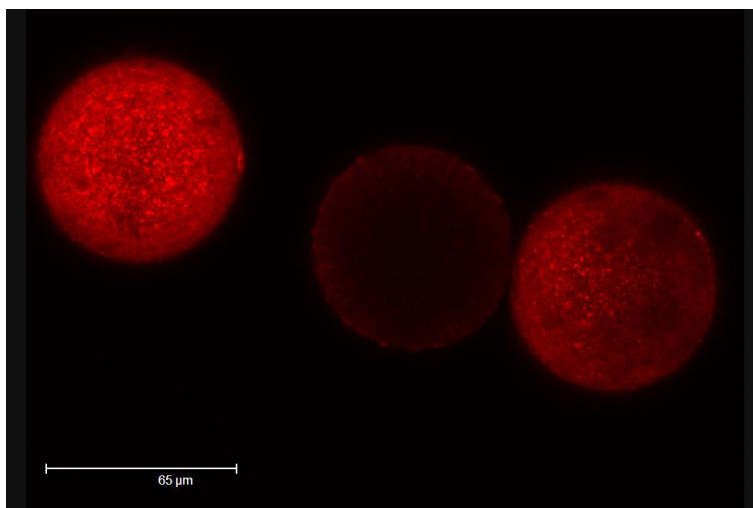


Figure 17 *Fluorescence micrograph showing polystyrene microspheres loaded with 610-nm quantum dots for optical barcoding synthesized by by the spraying suspension polymerization.* Image was acquired 30-days after microsphere preparation. This sample of microspheres was prepared by collaborators Vaidya and Couzis and the images were acquired by Kennedy and Batt 30-days after microsphere preparation and after shipping.

homozygous for allele 2 and heterozygous at the GABRA2 locus, respectively. The reaction mixtures were shaken for 20 minutes at room temperature and were then washed three times in water and stored in 50 μ L of water.

After hybridization, the beads containing the hybridized DNA were imaged using confocal microscopy. A microscope (Leica) outfitted with two excitation sources (633-nm, 488-nm) was used to simultaneously excite both the red and green chromophores (FAM and Cy5), which were covalently attached to the ssDNA at the 5'-end during synthesis (idtdna).

After verifying hybridization, the beads containing the hybridized DNA were pumped through the integrated flow cytometer at a rate of 2-uL/min, with a focusing ratio of $U3/U2=1.0$ and a sheath flow-rate of 18-uL/min. Voltage traces were acquired for 5-minutes, and these voltage traces were analyzed with matlab, as described above.

OPTICAL BARCODE FOR MULTIPLEXED DETECTION OF DNA

In the case of the flow-through instrument, the microfabricated flow cytometer, simultaneous detection of a large number of specific target DNA requires a cocktail of fluorescently-labeled beads that can be independently detected. In 2003 Quantum Dot Corporation claimed to demonstrate multiplexed detection of DNA by loading microspheres with quantum dots and surface-attaching fluorescent DNA [60]. The method was very appealing for our system because quantum dots would eliminate the need for multiple excitation lasers from our particle detector. However, upon preparing Qbeads following the method of Xu et al., we found the Qbeads were not time stable for longer than a few hours of storage. Briefly, the method consisted of purchasing commercially available carboxylated polystyrene microspheres and shaking them in a vial with quantum dots until the quantum dots had migrated into the microspheres. We were not the only researchers with limited success, and consequently, even five years later, quantum dot loaded microspheres are not commercially available.

Because microspheres were not commercially available to satisfy our multiplexing needs, we explored methods for creating our own microspheres in house. In particular, we successfully synthesized polymer microspheres using a microfluidic flow-cell (Figure 16). The spheres shown are about 25-um in diameter. To fabricate the microspheres, the top and bottom inputs contained mineral oil, and the center input contained water with 1% dissolved polymer. The water-oil surface interactions assembled the water into dispersed droplets. These were

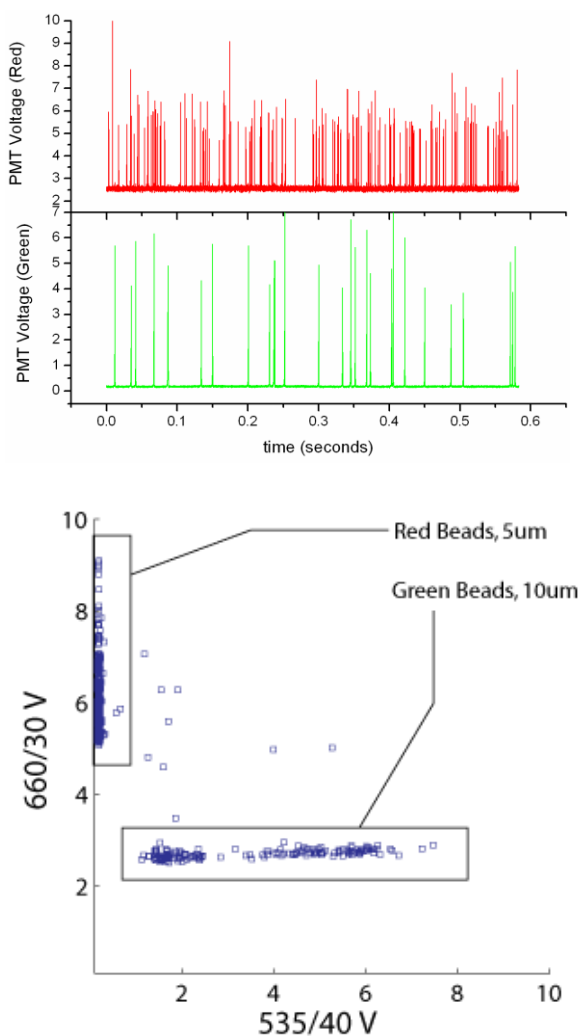


Figure 18 Two-color fluorescence detection using the flow cytometer on-a-chip. **Top:** Voltage-traces showing simultaneous two-color detection of red and green microspheres at a rate of over 100/sec. **Bottom:** Scatter-plot showing a total of 751 events from a 22-second recording. All events except for 11 are clearly resolved into either the green or red channel. This means the vast majority of events are single-bead events.

collected into a bottle of ethanol at the output of the flow-cell. The water is miscible with ethanol but the polymer is insoluble. Therefore, the polymer becomes formed into hard microspheres in a solution of 95% EtOH with a small delution of water. We can make different sizes of spheres and control the size, actually, by changing the height of the microchannel.

We worked briefly with [61] who developed a new method for preparing quantum dot loaded microspheres that exhibit superior brightness and time stability than the method of [60]. The new method involves a modified spraying suspension polymerization technique in which a mixture of styrene monomer and quantum dots is quickly polymerized after being sprayed from a nozzle. The method consists of adding a small amount of hydrophilic monomer, methyl methacrylate, to the styrene and quantum dot mixture prior to polymerization, yielding a hydrophilic microsphere surface that can be coated with streptavidin. To control the size distribution, the monomer solution can be sprayed not directly into hot water / PVA solution but into a column of steam. Quantum dot-loaded beads synthesized by this method were shipped to us and were subsequently imaged after 1-month of storage (**Figure 17**). The beads were pumped through our microfluidic flow cytometer, but the beads were very heterogeneous in size making it difficult to resolve them spectrally due to varying amounts of autofluorescence. However, we maintain the method of Vaidya and Cousiz is the method of choice for the preparation of quantum dot loaded microspheres and could be improved by the use of a microfluidic flow-cell similar to that which we have developed shown in **Figure 16**.

2.4 MOLECULAR BEACONS

The goal of this research was to develop QD molecular beacons that could be used for DNA detection assays. Although Kim and co-workers have reported the use of QDs for molecular beacons [41], we sought to evaluate different attachment chemistries as well as different quencher moieties to determine which combination would yield the best molecular sensor. Our initial approach to creating QD molecular beacons was to attach amino-labeled molecular beacon DNA to carboxyl-modified QDs. The molecular beacon DNA sequence was designed to hybridize with a 17-bp portion of the *Salmonella typhimurium invA* gene. One end of the DNA was labeled with Iowa Black FQ for FRET-based quenching of the QD during hairpin formation. Using the zero-length crosslinker, EDC, we were able to successfully attach Iowa Black FQ-labeled molecular beacon DNA to QDs and could visually observe quenching of QD fluorescence (**Figure 6**).

Different linkage strategies and compositions for QD molecular beacons were also explored. We used a popular alternative to

Molecular Beacon Name	Fluorophore / Quencher	Molecular Beacon DNA Sequence
Carb-IB	Carboxyl 525nm Qdot / Iowa Black	5' CGCTCGTGTTTATGGGGTCGTTGAGCG
Carb-Dabcyl	Carboxyl 525nm Qdot / Dabcyl	5' CGCTCGTGTTTATGGGGTCGTTGAGCG
SA-IB	Streptavidin 525nm Qdot / Iowa Black	5' CGCTCGTGTTTATGGGGTCGTTGAGCG
SA-Gold	Streptavidin 525nm Qdot / 1.4nm Nanogold	5' CGCTCGTGTTTATGGGGTCGTTGAGCG

Table 1 Summary of Quantum Dot Molecular Beacon DNA sequences.

The abbreviated names and compositions of the various molecular beacons are shown. We also used the alternative organic quenchers Iowa Black™ (Integrated DNA Technologies, Coralville, IA) and dabcyl. Since FRET-based quenching can also be achieved through interactions between fluorophores and gold surfaces [62] or gold nanoparticles [63, 64], we also developed a QD molecular beacon using 1.4 nm Nanogold as a quencher. The various QD-DNA linkage and molecular beacon quenching strategies that were used are illustrated schematically in **Figure 5**. The abbreviated names and a short description of each QD molecular beacon are shown in **Table 1**.

MOLECULAR BEACON DESIGN

The molecular beacon used in this study was designed using the nucleic acid manipulation software Vector NTI (Invitrogen, Carlsbad, CA). The molecular beacon was designed to hybridize to a 17 base portion of the *Salmonella*

typhimurium invasin gene (*invA*). Using Vector NTI and BLAST (www.ncbi.nlm.nih.gov/BLAST/) [65], a sequence was selected that did not have significant similarity to other reported sequences and had no predicted secondary structure formation. A 5 base “stem” was added to the 5’ and 3’ ends of this sequence that would enable stem-loop formation through internal hybridization to create the molecular beacon. The resulting sequence is 5’ **CGCTCGTGTTTATGGGGTCGTTGAGCG** 3’ where the bold, underlined portions represent the 5 base stem. To determine the effectiveness of this molecular beacon for sequence specific detection, two DNA sequences were chosen. The first, “invAF2” (5’TGCTGCTTTCTCTACTTAACAGTGC 3’) is complementary to the 5’ end of the *invA* gene, but does not overlap with the molecular beacon sequence. The second, “MB Comp” (5’AACGACCCCATAAACAC3’) is exactly complementary to the loop portion of the molecular beacon.

Molecular beacons were designed to use a quantum dot (QD) as the fluorophore and a variety of quenching moieties to provide fluorescence quenching. These included the Iowa Black FQ quencher (Integrated DNA Technologies), dabcyl, and 1.4 nm gold particles (Nanoprobes). For dabcyl and Iowa Black FQ quenched carboxyl-modified QDs the molecular beacon DNA was modified with a 5’ C6 amino modifier and either a 3’ dabcyl or Iowa Black FQ molecule. For Iowa Black FQ quenched streptavidin-modified QDs the molecular beacon DNA was modified with a 5’ biotin and a 3’ Iowa Black FQ. Finally, for Nanogold quenched molecular beacons the molecular beacon DNA was modified with a 3’ C6 amino modifier (for linkage to the Nanogold) and a 5’ biotin for linkage to streptavidin-modified QDs.

QUANTUM DOT—MOLECULAR BEACON SYNTHESIS

Several methods were used to attach quantum dots to the molecular beacon DNA backbone. As described above, multiple molecular beacon DNA molecules were synthesized with different attachment chemistries and quencher molecules attached to their 5’ and 3’ ends. The different molecular beacons that were synthesized included dabcyl- and Iowa

Black FQ-quenched carboxyl-modified QDs, Iowa Black FQ-quenched streptavidin QDs, and finally Nanogold-quenched streptavidin-modified QDs.

These represent a range of chemistries available for DNA-QD attachment, and include the most widely used quenchers for molecular beacons and other FRET-based assays.

A list of the DNA molecules used for QD molecular beacon synthesis is provided in **Table 2**, while the various molecular beacons that were synthesized are shown in **Table 1**.

Sequence Name	Sequence (5’ to 3’)
invAF2	5’ TGCTGCTTTCTCTACTTAACAGTGC
invAF2 - NH2 labeled	5’ NH2 - TGCTGCTTTCTCTACTTAACAGTGC
invAR4	5’ CGGCATCGGCTTCAATCAAGAT
Mol Beacon - NH2, DabcyI	5’ NH2 - <u>CGCTCGTGTTTATGGGGTCGTTGAGCG</u> - DabcyI
Mol Beacon - NH2, Iowa Black FQ	5’ NH2 - <u>CGCTCGTGTTTATGGGGTCGTTGAGCG</u> - Iowa Black FQ
Mol Beacon - Biotin, Iowa Black FQ	5’ Biotin - <u>CGCTCGTGTTTATGGGGTCGTTGAGCG</u> - Iowa Black FQ
Mol Beacon - NH2, Biotin	5’ Biotin - <u>CGCTCGTGTTTATGGGGTCGTTGAGCG</u> - NH2
MB Comp	5’ AACGACCCCATAAACAC

Table 2 DNA sequences used for molecular beacons, target DNA, and PCR primers. The tail sequences of the molecular beacons are shown underlined and in bold text. For each molecular beacon DNA backbone used, the 5’ and 3’ modifications are shown. The following abbreviations are used in the table: NH2 - amine group, FAM - fluorescein dye, MB comp - complementary sequence to the loop region of the molecular beacon.

For the first set of molecular beacons, Qdot ITK carboxyl-modified 525 nm quantum dots (Quantum Dot Corporation) were covalently linked to the 5’ amino linker of molecular beacon DNA modified with both dabcyl and Iowa Black FQ. The carboxyl surface groups of the QDs were activated with 1-ethyl-3-(3-dimethylaminopropyl) carbodiimide hydrochloride (EDC) (Hermanson, 1996) and allowed to react with the 5’ amino groups on the DNA. Approximately 100 pmol of Qdots were mixed with 300 nmol of EDC and 2 nmol of amino-labeled DNA in 400 µL of PBS in a 1 mL glass vial. The mixture was allowed to react for 2 hr at room temperature. Unreacted DNA and free EDC were removed from the QD-modified DNA by spin filtration in Millipore Microcon 50,000 molecular weight cut-off (MWCO) spin filters. Reactions were spun at 7,000 x g for 5 min and the retentate (QD-modified DNA)

resuspended in 400 μ L PBS while the flow-through was discarded. This was repeated two times and the final retentate was resuspended in 200 μ L of PBS.

For the second set of molecular beacons, biotinylated molecular beacon DNA was attached to Qdot 525 nm streptavidin conjugate (Quantum Dot Corporation) by the well-established streptavidin-biotin interaction (Hermanson, 1996). Approximately 100 pmol of streptavidin-modified QDs were mixed with 1 nmol of biotinylated molecular beacon DNA and 40 μ L of 10 mg/mL BSA in 400 μ L of PBS. The mixture was incubated for 1 hr, washed, and resuspended as described above for the carboxyl-modified QD-molecular beacons.

Finally, for preparation of Nanogold-quenched molecular beacons, mono-sulfo-NHS 1.4 nm Nanogold (Nanoprobes Inc.) was modified with amino-labeled molecular beacon DNA. Approximately 1 nmol of mono-sulfo-NHS Nanogold was mixed with 10 nmol of amino-labeled, biotinylated molecular beacon DNA in 300 μ L of PBS. The mixture was incubated for 2 hr at room temperature and then quenched with 10 μ L of 10 mM glycine to deactivate any remaining NHS on the surface of the Nanogold. The reaction was then washed two times with PBS in a Millipore Microcon 10,000 MWCO spin filter with centrifugation at 7,000 x g and was resuspended in 200 μ L PBS. 100 μ L of the resuspended nanogold was mixed with 10 pmol of Qdot 525 nm streptavidin conjugate, 40 μ L of 10 mg/mL BSA, and 400 μ L PBS. This mixture was incubated 1 hr at room temperature and was washed two times with PBS in a Millipore Microcon 100,000 MWCO spin filter at 7,000 x g. The final retentate was resuspended in 200 μ L PBS. All QD-molecular beacons were stored in the dark at 4°C and were used within 1 month of their initial synthesis.

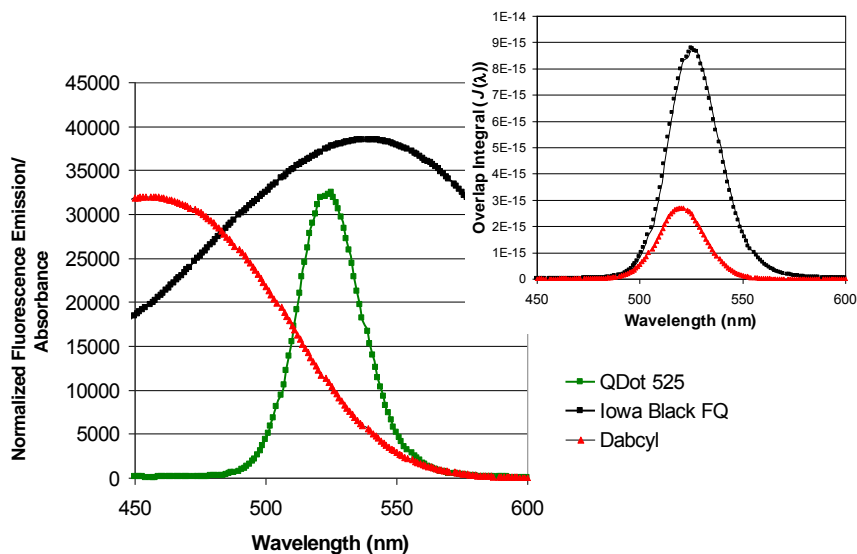


Figure 19 Normalized spectra for 525 nm Qdots (green), dabcyI (red) and Iowa Black FQ (black) and their overlap spectra (inset graph). The absorbance and emission spectra for the quenchers and Qdots, were normalized according to previous work by Medintz, et al. The overlap integral ($J(\lambda)$) was calculated using these normalized data over a step size of 1nm. For the inset graph, the overlap integral for dabcyI-Qdot 525 is shown in red, while the overlap integral for Iowa Black FQ-Qdot 525 is shown in black.

FLUORESCENCE MEASUREMENTS AND PARTICLE SIZING

To measure the fluorescence intensity of QD-molecular beacons we used both a standard microplate fluorometer (Tecan Genosys FL, Durham, NC) as well as the previously described microFLUIDICS DESKTOP (Cady N. S., 2005). Microplate fluorescence measurements of QD-molecular beacons were made with excitation at 360 nm and detection at 520 nm. Particle sizing was achieved using a Malvern Instruments (Worcestershire, UK) Zetasizer Nano ZS instrument. This instrument uses light scattering to measure the average hydrodynamic radius of particles in solution. Samples were placed in 0.5 mL plastic cuvettes and three measurements consisting of 10 runs with 5 sec duration were performed at 25°C. The instrument was standardized with 1 μ m polystyrene beads and particle size was reported as the average of the three measurements with an error measurement of one standard deviation.

CALCULATION OF FRET EFFICIENCY

The FRET efficiency for 525 nm Qdots with both dabcyI and Iowa Black FQ were calculated for a range of distances. This was done by first calculating the Förster Radius (R_0) as described by the above equation using previously described values reported by Clapp et al [41, 66]. A value of 2/3 was used for the orientation factor for dipole-dipole interactions (k) while a value of 1.40 was used for the refractive index of the medium (n). A value of 0.60 was used for the quantum efficiency of the donor (Q_d) as specified by Quantum Dot Corporation. The spectral overlap integral between the donor and acceptor ($J(\lambda)$), was found by using the Qdot emission spectrum (from Quantum Dot Corporation) and from empirically determined absorbance spectra of dabcyI and Iowa Black FQ. The overlap integral was calculated numerically using a 1 nm step size. The overlap integral for the 525 nm Qdot - Iowa Black FQ interaction was calculated to be 2.62×10^{-13} , and for the 525 nm Qdot - dabcyI interaction, 7.4×10^{-14} . The Förster Radius (R_0) for 525 nm Qdots - Iowa Black FQ was calculated to be 50.2 Å and for 525 nm Qdots - dabcyI, 40.6 Å. Once R_0 was calculated, the FRET efficiency (E) was calculated for a variety of distances from 1 nm to 20 nm using the previously described equation (above).

2.5 LIGASE DETECTION REACTION WITH SURFACE ENHANCED RAMAN DETECTION

MATERIALS

All chemicals and solvents were purchased at the highest purity grade available. For the SERS enhancers, 50 nm diameter silver colloid solutions were purchased from Nanocs (New York, NY). The buffer solution used was 10 mM phosphate-buffered saline (PBS) buffer solution (0.6 M NaCl, pH 7.6) and stored in a freezer until use. Poly(dimethylsiloxane) (PDMS) microfluidics were made using a Sylgard® 184 silicon elastomer kit (Dow Corning, Midland, MI). The thermostable ligase 9°N™ DNA Ligase was purchased from New England Biolabs Inc which included a buffer for the LDR reaction. All reactions were carried out at room temperature unless otherwise specified.

LDR REACTION

The oligonucleotide sequences of all the probes and templates used in these experiments are shown in Table 1. All DNA primers and templates were synthesized by Integrated DNA technologies and adapted by previous work done by [47]. During primer design, the fluorophore and the amine by which nanoparticles are attached were placed 14 bp apart. To maximize the RAMAN signal, the enhancer and fluorophore must be as close together as possible. The LDR reaction contained the following in 10 µL reaction: 25 pM of template, 100 pM of each primer, 1 µL of ligase, 1 µL of 10 X Buffer, and water to 10 µL. The LDR reactions used the following thermocycler program: 1) at 90°C for 2 min 2) at 90°C for 30 sec 3) at 50°C for 4 min 4) Repeat Steps 2-4 100 times.

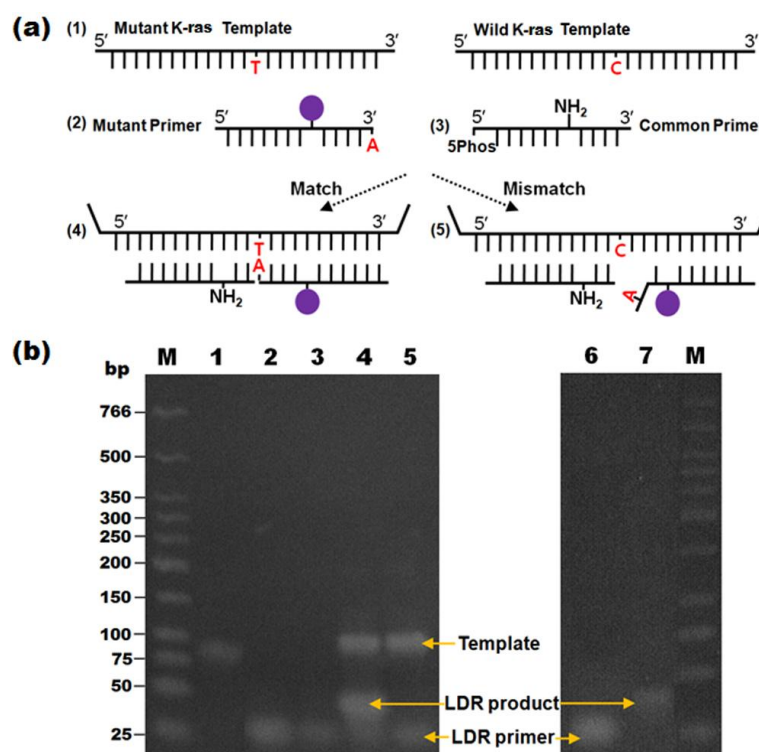


Figure 20 LDR Gel Shift Assay

LDR FUNCTIONALIZATION AND PURIFICATION

The LDR reaction mixture was treated with 2 μL of DMSO to lower the melting temperature of the single stranded template and primers and reduce post-ligation binding to each other. 100 picomoles of the NHS ester of thioctic acid was added to the treated LDR reaction and allowed to react for one hour. Thioctic acid was chosen as a linker due to its high affinity for Ag and greater stability than thiols when coupling oligonucleotides to nanoparticles[67]. The amine modification present in the primer is an amine modified deoxythymidine with a c6 spacer. The reaction mixture was then added to 200 μL of 50 nm Ag nanoparticles and allowed to react for 1 hr. After the reaction, the solution was put onto a 37 mL size exclusion column using Superdex 200 resin and flowed at 2 mL/min using DW eluent solution. The first elution peak by Abs280 was collected and determined to be the particles. Further evidence of purification is seen by the negative control where fluorophore conjugated DNA is exposed to the silver nanoparticles then purified. Very little signal is seen as compared to the experimental samples. The particles were then concentrated using a 30 kD spin filter, spinning at 2500 g for 1.5 min intervals and resuspending completely between spins. It is important to note that if the particles are not resuspended or are spun too hard, they will irreversibly stick to the filter membrane.

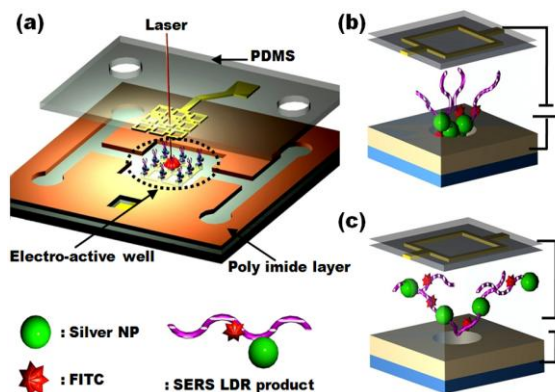


Figure 21 *Electroactive Nanowell Diagram*

GEL SHIFT ASSAY

An expected positive and negative LDR reaction were run on a 3% Low-Melt temp TAE agarose gel for 50 min at 200 V in a cold room and subsequently stained with ethidium bromide (**Figure 20**, Lanes 1-5) or directly (**Figure 20**, Lanes 6-7). LDR-SERS reactants and products were characterized via fluorescent imaging after ethidium bromide staining as compared to DNA fragments of known size (Lanes 1-5, **Figure 20**). [68] reported that the allelic probes can be designed to have unique lengths, so that the wild type and variant ligation products can be separated and detected on the basis of size. In this study, the allelic probes were labeled with fluorophores, enabling the ligation products to be additionally discriminated by the presence of fluorescence without being stained by ethidium bromide (lanes 6 and 7, **Figure 20**).

MICROFLUIDIC DEVICE

Figure 21 shows a schematic of the microfluidic device used here. As mentioned above, in addition to the sample delivery channels, the active element in the device are the electrokinetically active microwells which serve to rapidly concentrate the reaction products from the bulk solution phase into a confined volume for optical probing. Details of the fabrication are outlined in the work of our collaborators [69], however briefly the overall structure consists of three functional layers, namely, a lower substrate which contains the attraction electrode, a polyimide (PI) dielectric layer into which the channels and microwell were defined, and an upper electrode. The device was manufactured by first spinning positive and lithographically patterning photoresist S1813 (Shipley, Marlborough, MA) onto a Pyrex substrate to define the lower electrode pattern. Following this, 5 nm Ti/ 50 nm gold was evaporated and a lift off process carried out with 1165 photoresist stripper (Shipley Microposit) overnight, leaving the lower electrode on the glass surface. A two layer photoactive PI process was used to pattern the microchannels and wells as shown in **Figure 21**. The upper gold electrode was patterned on PDMS using a similar technique to that described by [70]. To bond the upper and lower surfaces, both layers were activated in oxygen plasma and the two halves were aligned and pressed together using our home-made aligner.

To record the SERS emission spectrum, the LDR-SERS products were concentrated in the microwell by applying the attraction potential. The approach uses electrokinetically active microwells to physically concentrate the bulk phase reaction product into a well defined volume for optical interrogation. For each of the measurements reported here, we take spectra from 3 different points in the 10 μm well (using a 2 μm laser spot size) and report the average measurement (with error bars to indicate the standard deviation). Further details on this concentration approach (including detailed comparison with other approaches) are available in this earlier work[71]. The excitation laser was focused at the microwell through the upper gold electrode patterned PDMS layer. In all cases a Hewlett–Packard 6234A dual output power supply and a Keithley 236 were used to apply and measure the electrical potentials.

RAMAN SPECTROSCOPY MEASUREMENTS

Raman measurements were made using an inVia Raman microscope spectrometer coupled to a Leica microscope. The experiments were conducted by focusing the excitation laser on the electro-active microwell. The 488 nm line of an Ar⁺ ion laser was used as optical excitation source and the scattered signal was collected by a Peltier-cooled CCD detector. A 50 X (NA=0.55) objective lens was used to focus the laser beam spot onto the sample surface with diameter of about 2 μm . Wave-numbers ranging from 1100 cm^{-1} to 1800 cm^{-1} were examined here.

III. RESULTS

3.1 PCR-BASED DETECTION MICROCHIP

We developed a PCR-based detection microchip consisting of two chambers integrated onto a single chip: the first chamber contains silicon pillars for DNA purification and the second chamber contains a meandering microchannel for PCR-based amplification. In the first chamber, silicon pillars are etched into a silicon microchip (1.5cm x 3cm) and each pillar is 10 μm x10 μm square, by 100 μm tall. Approximately 50,000 pillars are contained in each microfluidic channel, yielding an extremely high surface area to volume ratio. The pillars are coated with silicon dioxide (SiO₂), a surface which is commonly used for DNA purification in chaotropic salt-containing buffers. Previous work in our laboratory has demonstrated the effectiveness of these pillars for tube-free DNA purification from bacterial [12]. The second chamber included in the microchip has been designed for real-time PCR detection. The microfluidic PCR reaction chamber is designed to be cast in PDMS elastomer from a microfabricated silicon mold.

An integrated detection platform was designed and constructed for automated DNA purification and real-time PCR in a self-contained system. Individual components of the instrument were characterized separately. During testing, the pump was shown to be capable of pumping at flow rates from 1.7 $\mu\text{l}/\text{min}$ to 50 $\mu\text{l}/\text{min}$. Fluid flow rates were determined by pumping fluids into 50 μl graduated glass microcapillaries at known motor stepping frequencies for a given length of time. After the flow rate calibration of the instrument, the on-board microprocessor was used to drive the pump at known frequencies and times making it possible to determine volumetric accuracy in the graduated microcapillary tubes. The accuracy of the pumping rate was measured to be +/- 0.1 $\mu\text{l}/\text{min}$. An electrically actuated microvalve from Moog (East Aurora, NY) was used to direct fluid flow and

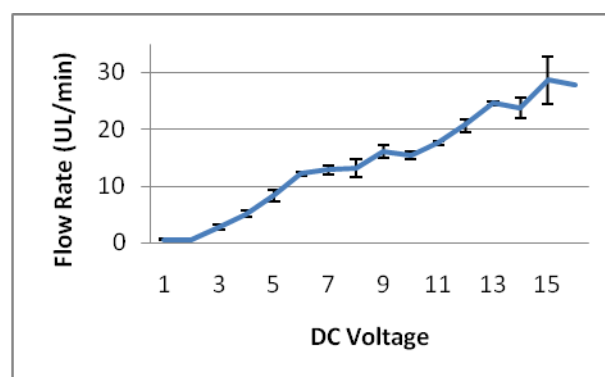


Figure 22 *Effect of DC Voltage on the flow rate of water driven by the uEHP.* 12 x 12mm EHPs were used to pump water using DC voltage. Two flow rate measurements were taken at each voltage and the entire test lasted for 160 minutes. Threshold voltage was determined to be 2.5VDC.

pressurize the system in preparation for thermal cycling. This is important for switching the direction of fluid flow between purification and PCR procedures on the chip and for preventing bubble formation during thermal cycling. Without pressurization, dissolved gasses and microscopic bubbles in the reaction mixture can increase in volume, especially during the 95°C portion of PCR thermal cycling. This results in bubble formation, causing increased light scattering that degrades the fluorescent signal from the real-time PCR reaction. Pressurization above 1 atmosphere reduces gaseous volume changes at high temperatures, preventing bubble formation. During testing of the fluidic system, the entire sample preparation procedure, including DNA purification, DNA elution and chip pressurization took approximately 15 min. The on-board TEC-based thermocycler was tested for its ability to rapidly and accurately cycle between the necessary temperatures for PCR. The average heating and cooling rates for this thermocycler were both 3.1°C/sec. Using cycling parameters of 95°C for 10 sec, 57°C for 15 sec and 72°C for 20 sec, an entire 40 cycle reaction could be completed in 35 min. In comparison, the ABI Prism 7000 real-time thermocycler that was used for validation experiments required 1 hour and 20 min while using the identical cycling parameters, nearly 4 times longer than our instrument. Combined with the 15 min needed for sample preparation, the entire process of preparation and detection took only 50 min with our system.

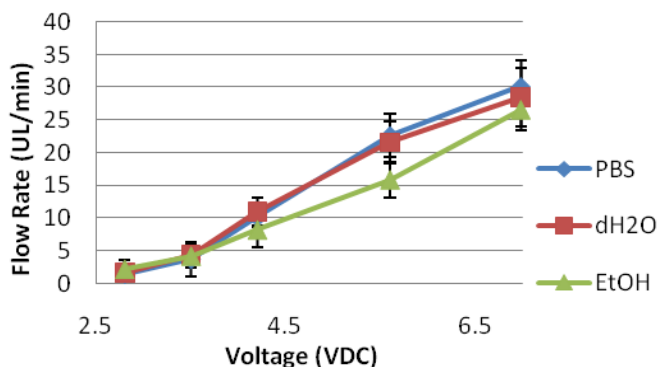


Figure 23 Effect of voltage on the flow rate with various solvents using the EHP technology.

The on-chip PCR conditions were optimized by addition of 5 units of extra Taq DNA polymerase and pre-treatment of the PCR chamber with 50µl of 10mg/mL BSA (data not shown). After optimization of the on-chip PCR conditions, we performed real-time PCR reactions using varying starting concentrations of template DNA.

MICROFLUIDICS DESKTOP MULTIPLEX

We have been constructing a multiplex detection instrument (**Figure 8**) similar to that used previously with the SYBR Green real-time PCR assay (**Figure 1**). This new instrument is based upon a Hamamatsu H9530 PMT detector, which can resolve 8-spectrally independent chromophores simultaneously. This detector has been incorporated into the newest version of our microFLUIDICS DESKTOP, and initial testing with PCR reactions have been performed with a two color (FITC, ROX) master mix (**Figure 9**). The curve shows “crosstalk” between the two fluorescent signals due to the broad-spectrum fluorescence signal of the organic dyes under observation bleeding into the adjacent windows of the detector. This challenge can be overcome by replacing the conventional organic dyes by narrow-spectrum fluorescence indicators, specifically quantum dots, as real-time probes in the multiplexed PCR assay.

MELTING CURVE ANALYSIS

During real-time PCR, the K-allele primer was amplified beginning at cycle number 17 while the R-allele primer was not amplified until cycle 32, indicating that the subject tested was positive for the K-allele and negative for the R-allele (Figure). The dissociation curves show peaks at 88C for the K-allele and 91C for the R-allele. The dissociation curve for the mixture containing primers for both alleles shows both peaks distinctly separated by 3C

(Figure). These results suggest the extendibility of our DNA extraction technique to human samples and the prospect of using melting curve analysis in a field portable device.

3.2 ELECTROLYTIC HYDRAULIC MICROPUMP

The goals were to fabricate EHPs with a wide range of fluid pumping rates and to characterize the pressure output and long term performance characteristics. We also sought to improve the electrode interface and to create an electronic control system to modulate fluid flow rate and volume.

The EHP pumps and control system were tested to determine their flow rates and reliability. We performed exhaustive testing of multiple pumping parameters. The testing parameters included:

- Flow rate analysis (minimum and maximum rates, sustained pumping)
- Pump calibration with different reagents (buffers, solvents)

During this effort, different configurations of EHP pumps were constructed and tested. Variation in the size of the respective electrolyte and reagent chambers was examined. The size of the chambers was varied from 6mm to 75mm and the chamber volume ratios varied from 1:1 to 1:3. In this manner we could systematically examine the effect of reservoir size and hydraulic advantage on the pumping rates and pressure.

Table 3. Relationship between pumping chamber diameter and maximum pumping pressure.

Electrolytic Chamber Diameter	Reagent Chamber Diameter	Max Pressure (kPa)
20mm	20mm	66
12mm	20mm	119
20mm	25mm	150
20mm	12mm	66
25mm	25mm	91

TESTING OF FLOW RATES

As an example, we measured the minimum and maximum flow rates on an EHP system with chamber sizes of 20x20mm. The chambers were filled with 0.93mL of fluid and voltages applied to induce the electrolytic process. The flow rate was measured volumetrically over time. The average maximum flow rate was 16 μ L/min for sustained flow powered at 7VDC (**Figure 24**). A variation in +/-0.5 μ L/min was observed over time. This fluctuation is in part due to the irregular bubble formation and lack of feedback control.

The minimum flow rate for this pump was 1.25 μ L/min at an applied voltage of 3V (**Figure 24**). The flow rates were maintained for 15 min or more and demonstrated a wide range in deliverable fluid flow rate. Notably, pumping at lower flow rates (1-5 μ L/min) resulted in more stable flow rate profiles, which can be attributed to more uniform bubble production within the electrolyte chamber. For both low and high flow rates, however, there is some variability in the absolute pumping rate over time.

We also tested the compatibility of the EHPs with various reagents and created calibration curves for flow rate vs. applied voltage for each reagent. Ethanol, phosphate buffered saline (PBS) and dH₂O were all pumped with EHPs and demonstrated repeatable pumping profiles (**Figure 23**). These calibration curves could be easily used with the electronic control system to provide defined fluid flow rates.

LONG-TERM TESTING

Long-term testing demonstrated that EHPs could be operated for 30 min per day for up to 5 weeks (using large volume reagent reservoirs). Although these tests showed that pumps continued to be operational for extended periods of time, it was noted that the electrolysis chamber lost pressure between subsequent tests. Therefore, re-pressurization was required during each test, resulting in a short (1-2 min) delay before fluid was expelled from the

pump. This further demonstrates the need for a feedback control system to monitor fluid expulsion and resulting flow rate.

PRESSURE TESTING

Pressure testing was performed to determine the maximum achievable pumping pressure and its relationship with the EHP hydraulic ratio (ratio of reagent chamber and electrolyte chamber surface areas). EHP outputs were attached to a pressure sensor during fluid pumping at 10.6V (approx. 30 μ l/min) and maximum pressure was measured upon device failure (fluid leakage). The maximum pressure for different chamber configurations is shown in **Table 3**. The maximum pressure of 150 kPa was obtained with 20 mm diameter electrolytic chambers and 25mm reagent chambers (a hydraulic ratio of 1.6:1).

GOLD ELECTRODE EHP TESTING

In the miniaturized gold electrode versions of the EHPs, the maximum flow rates for the gold electrode EHP devices were measured at 7.00 μ l/min, 4.03 μ l/min, 2.43 μ l/min, and 1.24 μ l/min for the applied voltages of 10V, 7.5V, 5.0V, and 2.5V, respectively. The linear relationship between the maximum and average flow rate and the applied AC voltage are represented by the coefficients 0.7552 μ l \cdot min⁻¹ \cdot V⁻¹ and 0.23467 μ l \cdot min⁻¹ \cdot V⁻¹, respectively.

Due to smaller volumes, the pumps only required 5 minutes of operation to deliver the reagent chamber fluid. The maximum flow rates (Figure 26) are achieved within the first two minutes of operation. Unlike its stainless steel counterpart, the gold electrodes were more susceptible to degradation over time. Annealing of the gold electrodes allowed us to double the electrode lifetime (from approx. 10 minutes to 20 minutes), and switching from DC to AC operation allowed us to further extend that lifetime to 40 minutes. The EHP outputs were attached to a pressure sensor and monitored real-time via LabView in order to measure the maximum pressure (343 kPa) the device is able to sustain before leakage failure was determined. This pressure exceeds the maximum pressure obtained from the larger stainless steel EHPs, suggesting that a stronger seal at the device inputs, outputs and electrodes can be formed using microfabricated techniques.

EHP technology is low-cost and disposable with a high level of reproducibility. The polymer-based fabrication methods are compatible with standard microfabrication technologies, making it possible to directly integrate these pumps with lab-on-a-chip systems. While the stainless steel electrodes were effective, the deposition of the gold electrodes by processes compatible with standard silicon processing allows us to move forward with a more integrated, scalable manufacturing process.

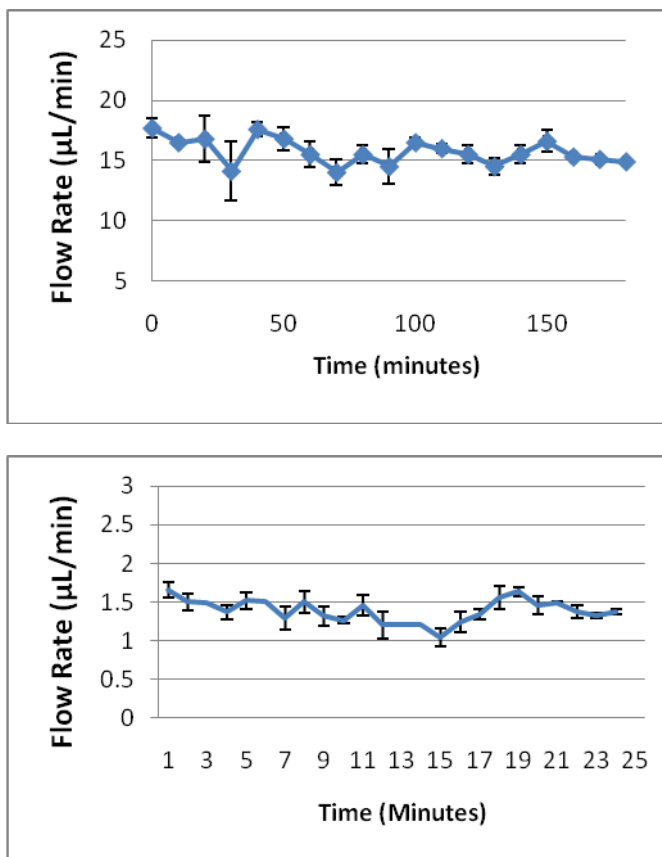


Figure 24 *EHP flow rate versus time.* a) Top: A 20mm diameter EHP pump run at a voltage set at 7VDC with stainless steel pins for electrodes. b) Bottom: A 20mm diameter EHP pump run at the lowest flow rate. Voltage was set at 3VDC with stainless steel pins for electrodes.

3.3 INTEGRATED FLOW CYTOMETER

MANIFOLD DESIGN AND OPERATION

The manifold was constructed from two complementary pieces of microfluidics housing. The dimensions of the manifold are $h=125\text{-}\mu\text{m}$, $w_1=125\text{-}\mu\text{m}$, $w_2=50\text{-}\mu\text{m}$, and $w_3=50\text{-}\mu\text{m}$, as illustrated in Fig. 1a. The sample was pumped into the first input at volumetric rate U_1 , and focusing fluids were pumped into the second and third inputs at volumetric rates U_2 and U_3 , respectively, as illustrated in Fig. 1b. The flow-cell was operated at Reynolds number $Re=2.72$, corresponding to a total volumetric flow-rate of $U_0 = 20.4\text{-}\mu\text{L}/\text{min}$ and an average fluid velocity of $\bar{v}_0=2.20\text{-cm}/\text{s}$, for all measurements. Also, the ratio of sample fluid to total fluid was fixed at $U_1/U_0 = 1/10$.

MANIFOLD SIMULATIONS AND IMAGING

The concentration distributions of fluorescein and rhodamine were calculated over the volume of the manifold using ANSYS Multiphysics Computational Fluid Dynamics Software. Our simulations predicted that the sample would become sheathed on all sides in a cylindrical manner as shown in **Figure 13**, where the ratio of the rate of the top focusing fluid to the rate of the bottom focusing fluid was $U_3/U_2 = 1.5$. The focusing takes place in two steps: at the first junction, the sample is impinged from below by focusing fluids from the bottom layer, and at the second junction, the sample is impinged from above by focusing fluids from the top layer. A vertical slice through the center of the channel along the direction of flow is shown in **Figure 13**.

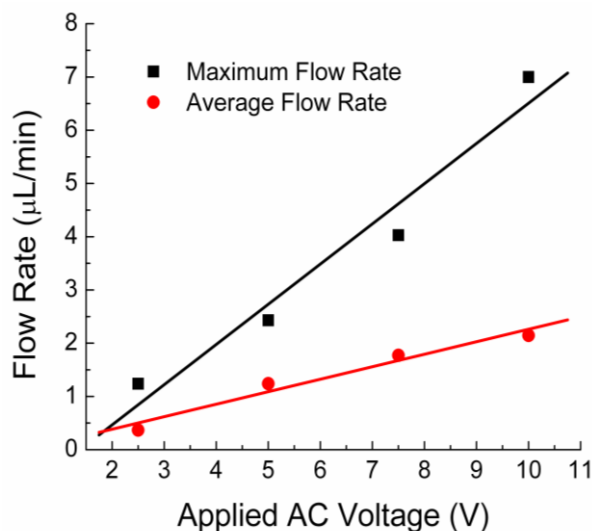


Figure 25 EHP flow rate versus Applied AC Voltage. A 3mm diameter gold electrode EHP pump was operated at different AC voltages (5, 7.5, and 10V, at 10Hz), and the maximum flow rates and average flow rates over a period of 5 minutes were recorded.

The distribution of fluids at the output of the manifold was imaged by scanning through the depth of the channel with confocal microscopy. The focusing ratio, U_3/U_2 , was varied, and several images were obtained. For small values of U_3/U_2 , the sample was positioned near the top of the microchannel, whereas for large values of U_3/U_2 , the sample was positioned near the bottom of the microchannel as shown in **Figure** . In the case of $U_3/U_2=1.5$, the sample fluid was sheathed on all sides and was positioned near the geometric center of the microchannel.

Similar behavior was exhibited by the experimental and simulated images not only regarding the vertical position of the focused stream but also regarding the shape. For example, when the top focusing fluids were applied at a rate similar to the bottom sheath fluids, the fluorescein stream took the form of an ellipse with a height of approximately twice its width. When the top focusing fluids were applied at a higher rate than the bottom focusing fluids, the fluorescein stream took the form of an isosceles triangle with its base lying along the bottom wall of the microchannel, as in **Figure** .

Images were processed and then measured to yield the vertical position of the center of mass of the fluorescein-containing fluids. For this purpose, an image analysis program was written in MATLAB so that all images were processed and analyzed using the same sequence of steps. Our program consists of four procedures: (1) image registration, (2) spectral unmixing, (3) depth-dependence compensation, and (4) measurement of the center of mass of the fluorescein-labeled fluids. The first procedure aligns the images to a common origin; the second and

third procedures restore the images of two optical effects: spectral bleed-through and depth-dependence of fluorescence intensity; the fourth procedure provides a quantitative measurement describing the location of the focused sample.

An image registration procedure was developed to locate the geometric center of the microchannel in each image. This provided a reference point to which the various images were subsequently aligned and was necessary because the microscope drifted slightly during the time between the acquisition of successive images. The procedure first detected the walls of the microchannel using the Sobel Edge Operator. Next, the channel dimensions were approximated as a rectangle by fitting the Sobel-detected edges with the best-fit horizontal and vertical lines. The height of the channel was measured to be $h=130\pm 2$ μm and the width of the channel was measured to be $w=128\pm 2$ μm . The uncertainty in the measurement of h was a consequence, in part, of the distance in depth between successive scan-lines, $\Delta y=1$ μm . The uncertainty associated with locating the bottom wall, where the image was relatively dim, was greater than the uncertainty associated with locating the top wall. The uncertainty in measuring w arose because the fabricated microchannel was not completely square; specifically, the microchannel was slightly wider at the top than the bottom. The error was estimated by calculating the standard deviation of the Sobel-detected edge pixels about the fitted line, as described in the methods section.

Cross-talk between the red and green channels of photodetection was removed by a linear spectral unmixing procedure. This procedure corrected for the partial overlap in emission spectra of rhodamine and fluorescein, separating the two contributions from the acquired spectrum and allowing for the calculation of the contribution of each dye to each pixel's intensity.

The decay in the brightness of the image along the depth of the microchannel was corrected using a mathematical correction procedure.

The center of mass of fluorescein was calculated according to the usual formula as described in the methods section. This calculation was performed on both the experimental images and the simulations. The error associated with the center-of-mass measurements was dominated by the error in measuring the position of the channel walls, which was discussed in section 3.3, and was therefore independent of U_3/U_2 . The stated values of x_{CM} and y_{CM} are both normalized by the height, h , and width, w , of the microchannel as measured from the experimental images during the image registration procedure.

The center of mass of fluorescein was measured for images obtained using a range of U_3/U_2 . The experimental values of y_{CM} are scatter-plotted in Figure , and the simulations are represented by a dashed curve on the same plot. The curve representing y_{CM} according to the simulations is antisymmetric about a point-of-inflection which occurs at $U_3/U_2 = 1.5$; the curve decreases monotonically, is steep near the point of inflection, and levels off at extreme values of U_3/U_2 . The experimental data follow all of these trends, verifying the accuracy of our simulations.

One might expect the point of inflection of y_{CM} to occur at $U_3/U_2=1.0$, corresponding to the case where focusing fluid is applied to the upper and lower focusing inputs in equal amounts. In addition, one might expect the distributions corresponding to focusing ratios of $U_3/U_2= 190$ and $U_3/U_2=.012$ to be mirror images of one another, since the flow-rates applied to the upper and lower inputs have simply been switched. However, for these cases, when the flow-rates applied to U_3 and U_2 are switched with one another, the

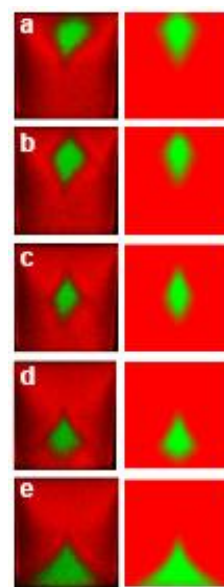


Figure 26 *Fluorescence micrographs and simulations showing the distribution of the fluids at the output of the manifold.* Confocal microscopy images are shown at left and simulations are shown at right for U_3/U_2 equal to a) 0.012, b) 0.20, c) 1.5, d) 11, e) 190

two resulting distributions vary considerably in morphology, as shown in **Figure** . This asymmetry is a consequence of the focusing taking place in two stages and shows the importance of the order of the inputs when working with laminar flow device.

COUNTING OF MICROSPHERES

The integrated flow cytometer was tested for its ability to simultaneously count fluorescent microspheres of two colors, red and green. During a data acquisition time of 22-seconds, 751 events were recorded. Of these, 740-events correspond to single-bead events which are clearly discernable as either red or green on a scatter-plot (**Figure 4**). The scatter-plot was obtained by subtracting the peak voltage value from the baseline voltage value for each photon-burst event. In this case, some of the 740-events may not correspond to single-bead events but two-bead events in which two-red or two-green beads are simultaneously illuminated by the beam. Since the probability of simultaneous illumination of two-green or two-red microspheres is the same as that of one-red-plus-one-green, we can conclude that approximately 718 out of the 751-events (over 95%) corresponded to single-bead events.

ALLELE SPECIFIC HYBRIDIZATION ASSAY

The beads used in the allele-specific hybridization assay were imaged by confocal microscopy (**Figure 15**). The two beads are clearly resolveable based on the red color (allele 2) and green color (allele 1) of the halo of fluorescent DNA on the bead surface. Clearly, the hybridization of short dna sequences at room temperature is specific for single-nucleotide mismatches.

The beads used in the allele-specific hybridization assay were analyzed using the microfabricated flow cytometer and the results are shown in **Figure 28**. Here, lot 7 refers to beads specific to the green-labeled target dna added to a heterogeneous mixture of red and green target dna, while lot 8 refers to beads specific to the red-labeled target dna added to a heterogeneous mixture of red and green target dna. Unfortunately, we were unable to conclusively resolve the two populations using our integrated flow cytometer. As shown in **Figure 28**, we were able to count thousands of DNA-bound beads in a period of five minutes. Looking at the histograms in **Figure 28**, the mean response is about 0.5V higher in the green-channel for the green-labeled beads than for the red-labeled beads. However, their was no resolveable difference in the red channel. We believe our inability to conclusively resolve the red-labeled dna from the green-

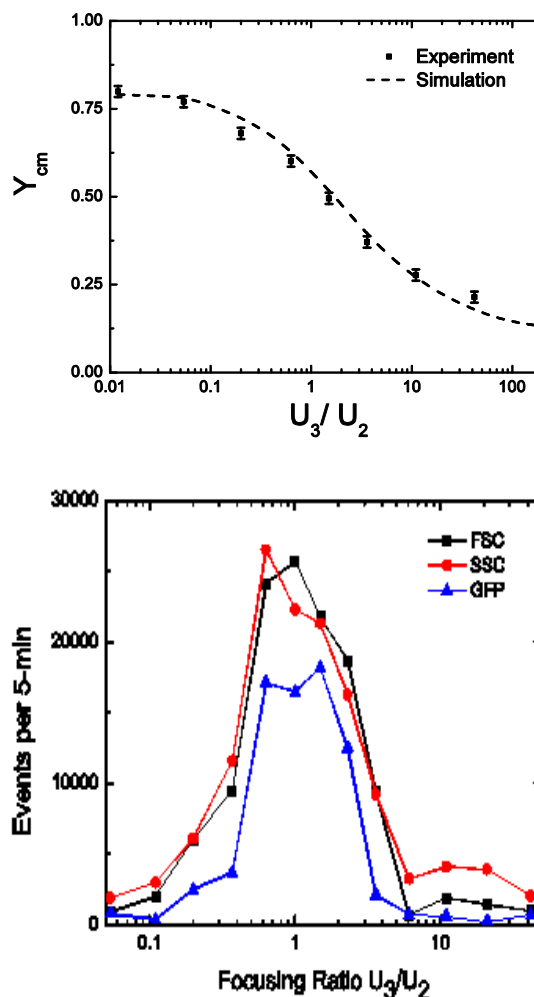


Figure 27 Effect of the ratio of the flow rates of the focusing fluids on the vertical position of the focused stream in the hydrodynamic focusing manifold and on the counting rate of beads in the integrated flow cytometer. **Top:** Plot showing the vertical position of the center-of-mass of the fluorescein-labeled fluid against the ratio of the flow-rate of the upper sheath flow to the flow-rate of lower sheath flow, U_3/U_2 . **Bottom:** Plot showing the count rate of 2-um polymer microspheres in the integrated flow cytometer (**Figure 4**) against the ratio of the upper focusing fluid to the lower focusing fluid. The same set of events were digitally analyzed by triggering on the 45° scatter (FSC), 135° scatter (SSC), and green fluorescence (GFP) channels.

labeled dna with the integrated flow cytometer may be a consequence of our choice of low-voltage PMTs, which were originally intended for long integration time measurements on the microfluidics desktop and were not intended for use in a flow cytometer.

3.4 QUANTUM DOT MOLECULAR BEACONS

To confirm modification of QDs with molecular beacon DNA, we measured the average diameter of the QD molecular beacons and compared them to unmodified QDs and QD conjugates using a laser-based particle-sizing instrument (Malvern Zetasizer Nano ZS) that has previously been used to measure nanometer sized particles [72, 73]. Because the measured particles are in aqueous solution, these measurements represent the average hydrodynamic diameter of the particles. Light scattering measurements demonstrated an increase in hydrodynamic radius after modification of QDs with molecular beacon DNA. Unmodified carboxyl-QDs had an average hydrodynamic radius of 7 ± 2.2 nm and increased to between 13.5 ± 3.2 and 18 ± 6 nm after modification with various DNA molecules. As expected, these measurements showed that Qdot streptavidin conjugate was significantly larger (15.7 ± 3.7 nm) than the Qdot ITK carboxyl QDs (7 ± 2.2 nm). These measurements agree with the manufacturer's specifications (Quantum Dot Corporation) that Qdot ITK carboxyl QDs are approximately 5 nm in diameter and the streptavidin conjugate is between 10 and 15 nm in diameter. The larger diameter of the streptavidin conjugate is due to the attachment of large, approximately 4 nm diameter [74] streptavidin proteins to the QD surface. Although we could not resolve differences in diameter between DNA-modified and unmodified Qdot streptavidin conjugates, there was a 6-fold increase in hydrodynamic radius between DNA modified (73 ± 16 nm) and unmodified (11 ± 2.4 nm) SA-Gold beacons. This increase could be due to aggregation of particles in solution, or to cross-linking of particles during attachment of the Nanogold-DNA to the Qdot streptavidin conjugate.

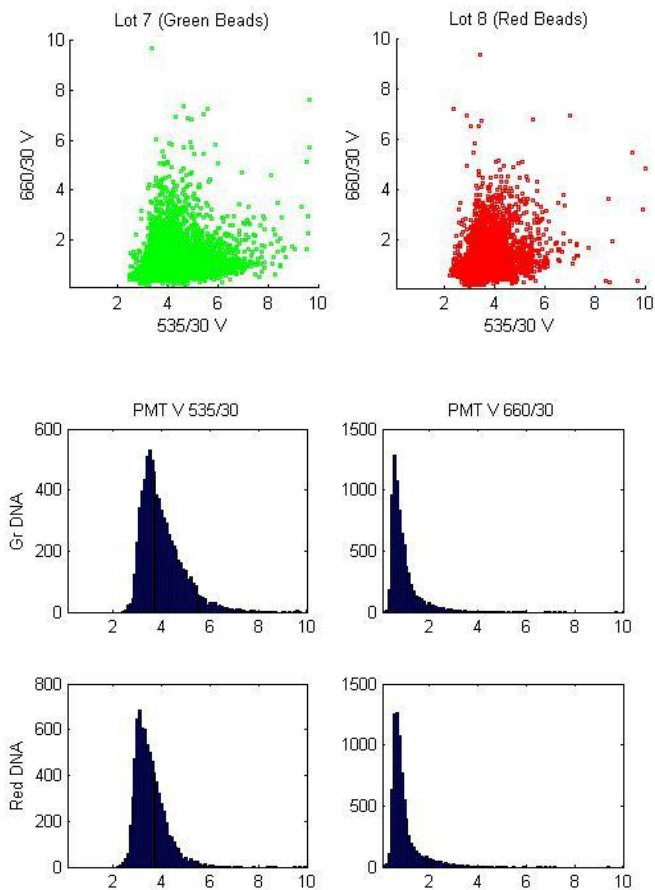


Figure 28 Results of analyzing the allele-specific hybridization assay using the microfabricated flow cytometer. **Top:** Scatter-plot showing the red vs. green fluorescence levels of about 7,000-events collected in 5-minutes. The beads plotted at left were specific for the target dna labeled with the green chromophore, whereas the beads plotted hybridized to red DNA. **Middle:** Histograms showing the number of photon-burst events at various PMT voltages for the beads bound to green DNA. **Bottom:** Histograms showing the number of events at various PMT voltages for the beads bound to red DNA.

To quantitatively compare the effectiveness of the various QD molecular beacons for biosensing, we measured the fluorescence intensity of molecular beacons mixed with complementary and non-complementary DNA. Fixed concentrations of each of the different QD molecular beacons (approximately 2 pmol for each) were mixed with 200 pmol of complement DNA (MB comp) or non-complement DNA (invAF2). The fluorescence intensity of each mixture was measured and then normalized to the fluorescence intensity of QD molecular beacons without added DNA. The results of this experiment are shown in **Error! Reference source not found.**. The results of the DNA hybridization-based unquenching of QD molecular beacons demonstrate that there are clear differences between the attachment methods used to link the molecular beacon DNA to the QDs, as well as differences in the effectiveness of different quencher moieties. When the same quencher (Iowa Black FQ) was used with different attachment strategies (covalent amino-carboxy versus streptavidin-biotin) a notable difference was seen in hybridization-based

unquenching. The covalently linked molecular beacons yielded a 3.3-fold increase in fluorescence while the streptavidin-biotin linked beacons yielded only a 2.1-fold increase in fluorescence. When comparing different quencher moieties, it was clear that the Iowa Black FQ quencher was a better quencher than dabcyI. We used covalent amide linkage for both Iowa Black FQ and dabcyI-labeled molecular beacons. The Iowa Black FQ labeled beacon, however, yielded a 3.3-fold increase in fluorescence (after hybridization with target DNA) whereas the dabcyI labeled beacon yielded only a 1.1-fold increase in fluorescence. This difference

could be due to multiple effects including differences in the ability of dabcyI and Iowa Black FQ to effectively quench QDs. In another comparison SA-IB beacons (2.1-fold increase) demonstrated a similar amount of activity to SA-Gold beacons (1.9-fold increase). This demonstrates that Nanogold may have similar quenching properties to Iowa Black FQ in this application.

To better understand if fluorescence unquenching of QD molecular beacons was due to DNA hybridization, we performed additional particle sizing measurements. Both carboxyl-QDs and streptavidin-QDs linked to Iowa Black FQ molecular beacon DNA were mixed with 200 pmol of complement DNA (MB comp) and their average particle size was measured with the Malvern Zetasizer Nano ZS instrument. Molecular beacon modified and unmodified QDs were also measured for comparison (**Figure 29**). These results demonstrate that the average hydrodynamic radius of the QD molecular beacons increased upon addition of complementary DNA. The increase in diameter is likely due to hybridization of the molecular beacon DNA with the complement DNA, resulting in an extended DNA structure. For Carb-IB beacons, the average hydrodynamic radius was measured at 13.5 ± 2.8 nm and increased to 15.7 ± 3.8 nm upon addition of complement DNA. For SA-IB beacons the hydrodynamic radius increased from an

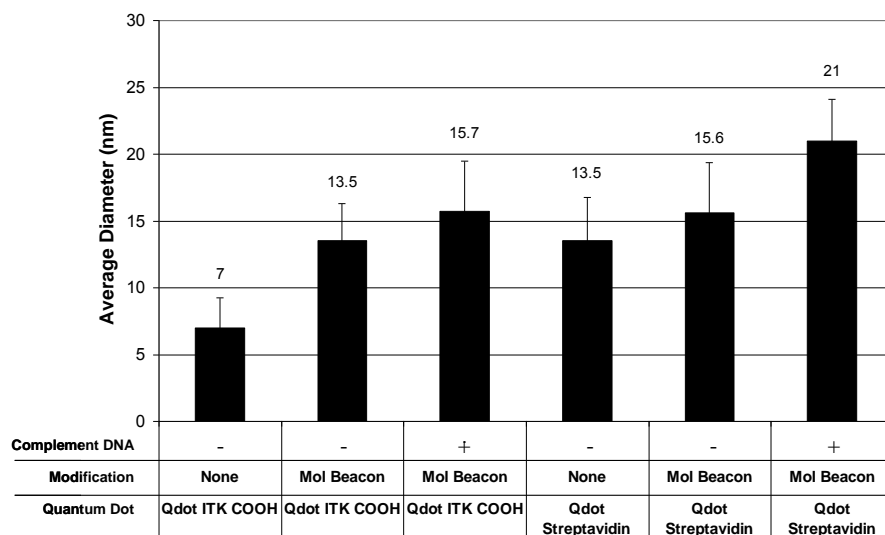


Figure 29 Particle sizing measurements of QD molecular beacons both alone and hybridized to complement DNA. Approximately 2 pmol of each QD or QD molecular beacon was measured in PBS buffer in a Malvern Instruments Zetasizer (Worcestershire, UK). To some samples, 200 pmol of complement DNA (MB comp) was added to 2 pmol of both Carb-IB and SA-IB beacons to measure changes in hydrodynamic radius due to DNA hybridization. Each measurement is the average of three separate measurements and the error bars represent one standard deviation.

average of 15.6 ± 3.7 nm to 21 ± 3.1 nm upon addition of complement DNA. This represents a 2.2 nm increase in hydrodynamic radius for the carboxyl QD molecular beacons and a 5.4 nm increase for streptavidin QD molecular beacons. The difference in measured diameter for the Carb-IB beacons, however, is within the standard error, and therefore may not be significant. Taken with the large increase in diameter for the streptavidin QD molecular beacons, however, these data could suggest that fluorescence unquenching is caused by hybridization of complement DNA that opens the beacon hairpin and spatially separates the QD from the quencher.

3.5 LIGASE DETECTION REACTION WITH SURFACE ENHANCED RAMAN DETECTION

DESCRIPTION OF SERS ENHANCED LDR REACTION

As mentioned in the introduction, we report here the development of a new reporter system for LDR based SNP detection reaction based on the use of surface enhanced Raman spectroscopy (SERS). The SERS effect is related to the phenomenon of plasmon resonance, wherein metal nanostructures exhibit a pronounced optical resonance, due to the collective excitation of conduction electrons in the metal, in response to incident electromagnetic radiation [75]. The plasmons result in a significant localized enhancement in the magnitude of the electromagnetic field surrounding the particle [76]. SERS active molecules located in the near field region of the optical nanostructures are therefore exposed to a larger electromagnetic intensity than that of the excitation light and thus enhancing the strength of its Raman scattered light. Most current SERS-based detection schemes involve the immobilization of the fluorophore labeled nucleic acids on a solid surface [53, 75, 76]. The SERS spectra are then generated based upon the proximity of the DNA and its fluorophore to the surface. Challenges with surface tethered systems include steric hindrance (and therefore a limitation in the accessibility of the target DNA) and the longer reaction time required for heterogeneous reactions. The advantage of the electrokinetically active microwell used here is that it enables active mixing to enhance the rate of binding between the SERS enhancers and the biomolecular targets as well as rapid concentration of the product for surface phase optical interrogation and enhanced sensitivity. It is important to mention that this is not the only method by which solution phase sensitivity could be increased, as a number of researchers have demonstrated the use of unique nanoparticle shapes [77] and assemblies [54, 78], resonance effects [79] and multiple wavelength interrogation [80] to enhance sensitivity and specificity. We note however that many of these effects could be used in conjunction with our technique for further enhancement.

In our approach, a nanoparticle Raman enhancer is incorporated directly into one of the LDR probes allowing us to perform the reaction homogeneously. **Figure 7** illustrates an overview of the SERS enhanced SNP-LDR reaction developed here. For simplicity a single set of PCR products are presented with two LDR probes. As is shown one LDR probe is internally modified to contain a fluorophore reporter and the other is internally modified with an exposed amine group. Following enzymatic ligation the exposed amine group reacts with a single silver nanoparticle as shown. If the two fragments match exactly the template sequence, the ligase will ligate them and the fluorophore and Raman enhancer are held in close proximity. Since the Raman enhancement is dependent upon the distance between the fluorophore and the nanoparticle, a strong SERS signal can be detected in the case where positive ligation occurs. In the case where a base pair mismatch exists the probes are not ligated and the fluorophore's Raman spectrum cannot be detected.

LDR based detection of point mutations in the K-ras oncogene. The efficacy of the LDR primers against their respective SNP targets were initially tested by using traditional gel electrophoresis (**Figure 20**). Each LDR reaction contained the amplified template DNA, the wild type or mutant LDR primer with a fluorescein modified deoxythymidine tag, and the common LDR primer. For the upstream primer and downstream primer, a band of the predicted size (20 bp) was observed at lane 2 and lane 3. As shown in **Figure 20b**, lane 2 was brighter than lane 3 with the same molarity because the mutant LDR primer (lane 2) contained the fluorophore. To verify the presence of the expected LDR product, two LDR reaction products reacted using the mutant template (MT, lane 4) and wild type template (WT, lane 5). For the positive sample, the band of LDR reaction size (40 bp) was observed

(lane 4) because the two fragments match exactly to the template sequence, resulting in the generation of a longer oligonucleotide, compared to the starting primers. For negative control (lane 5), however, a band of the expected LDR reaction size (40 bp) was not detected since the mutant primer and WT template were mismatched at the discriminating base of the upstream primer. After the LDR reaction, in order to obtain the higher SERS detecting sensitivity, the reacted samples were purified by size exclusion column.

Electroactive microwells for enhanced SERS signal detection. The current chip (**Figure 21**) comprises a glass substrate with lithographically patterned electrodes and is a modification of that presented in Huh et al. The substrate and electrodes are covered with an electrically insulating polyimide layer into which 10 μm diameter wells are etched. To deliver nanoparticles to the wells, a microfluidic structure is then defined in PI using standard lithography techniques. After completion we align and bond the PDMS fluidics to the bottom substrate such that the wells align with the spaces in the upper electrodes. By applying electric potential between the upper and lower electrodes, we can concentrate the solution phase targets into the wells as they flow over them. Once concentrated, the well can be interrogated optically through the upper PDMS as shown in **Figure 21**. When the SERS active LDR products were introduced into the chip via two inlet ports into the chamber, concentration was performed by applying potential of 1.5 V. This concentration step was found to increase the reproducibility and intensity of the SERS signal to the point where the spectrum could be recorded in as little as 15 s.

On-Chip LDR-SERS detection of point mutations in the KRAS oncogene. In this study, SERS detection was carried out using LDR reaction of low-abundant DNA point mutations in KRAS oncogenes with the allelic composition evaluated at one locus. As mentioned in the introduction, this oncogene has been associated with a variety of cancers including lung, colorectal, and pancreatic malignancies. To characterize the reaction experiments were conducted using the K-RAS mutation. In our first series of experiments, a downstream primer containing the amine was reacted with the NHS ester of thioctic acid (**Figure 7**). The resulting chemical reaction served as a linker between the silver nanoparticles and the DNA primer. The resulting downstream primer was then introduced into an LDR reaction containing the upstream primer and template. In this case the LDR reaction failed. After subsequent testing, it was found that the ligation reaction would not proceed with the nanoparticle attached to the primer so close to the ligation site. Through these initial results, we confirmed that pre-ligation chemistry and post-reaction purification were both important to successful detection.

For the on-chip assays, the LDR products described above were introduced into the chip via their respective inlet ports into the central chamber (**Figure 21**), where the concentration was performed, at a

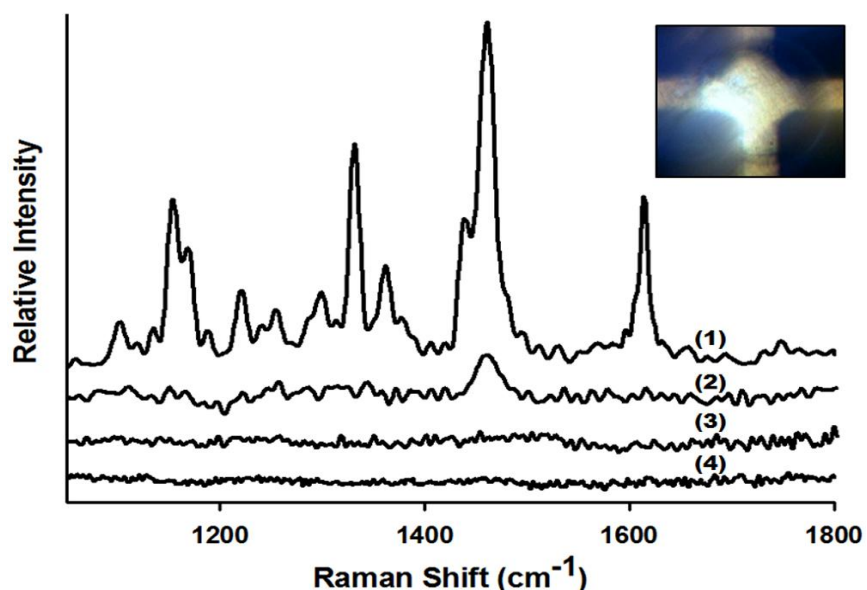


Figure 30 SERS spectra collected on-chip for (a) positive sample containing FMdT-labeled LDR-SERS products by the mutant template (denoted as FMdT-labeled MT), (b) negative sample reacted by wild type template, (c) control sample containing silver particles and DNA and (d) background control sample containing silver particles and linker. The concentration of each SNP is 100 μM .

flow rate of $5 \mu\text{L s}^{-1}$. After filling the SERS active LDR products were attracted into the wells for 15s at an applied potential of 1.5 V. To obtain the SERS signal, the excitation laser was focused at the microwell and the spectrum recorded integration time set to 15 s. In general, chip regeneration could be accomplished by reversing the polarity and rejecting the contents back into the chamber where they can be washed out. Here however a new device was used for each of the different experiments in order to avoid the potential for cross contamination. **Figure 30** shows the SERS spectra collected on-chip for (a) positive sample containing fluorescein modified deoxythymidine-labeled LDR-SERS products by the mutant template (denoted as FMdT-labeled MT), (b) negative sample reacted by wild type template, (c) control sample containing only silver particles and the DNA and (d) background control sample containing silver particles and linker. MT depicts the mutant, functionalized LDR reaction which was expected to show peaks indicative of the dye. As can be seen in Fig. 4, our results show that almost no detectable Raman signal was observed from the control sample for random adsorption of the DNA to the particles, nor from background control sample. As expected, Fig. 4a shows the correct spectroscopic fingerprints corresponding to FMdT-labeled dye suggesting positive detection. In the negative sample the LDR-SERS diagnostic peaks were much weaker suggesting the reaction was successful. Based on these results, we used the 1610 cm^{-1} peak as diagnostic of a successful ligation reaction since it is prominent in the mutated spectrum and completely lost in the wild type spectrum the 1610 cm^{-1} . The remaining peak at 1460 cm^{-1} in the wild type sample, is likely due to fluorescence from non-specific binding of the unligated primers. The large difference in the melting temperature of the primers as compared to the ligated LDR product meant that even at room temperature a significant difference was observed in the SERS spectra of the two samples.

To examine the detection threshold of our reaction and to verify the ability for quantitative analysis, we next conducted a series of experiments at different template concentrations. **Figure 33** shows the SERS spectra of FMdT-labeled MT in a microwell for various concentrations of reaction products of (1) 100 pM (2) 50 pM (3) 40 pM (4) 20 pM and (5) 10 pM. As expected, the intensity of the Raman peak decreases concomitantly with decreasing the concentration of LDR-SERS products. Consistent with the technique used by Lee et al, the concentration response was quantified by observing the change in the area of the SERS peak at 1610 cm^{-1} . The results are plotted in **Figure 33** and fitted to a linear curve (correlation coefficient: 0.993). As can be seen, below 20 pM the main diagnostic peak could not be detected and thus we omitted the 10 pM result from the corresponding calibration curve. Based on this result we report a limit of detection of 20 pM with this approach.

IV. CONCLUSIONS

4.1 PCR-BASED DETECTION MICROCHIP

In an improvement over other systems, our device presents a fully automated method of purifying DNA from bacterial cells and preparing samples for PCR-based detection. This approach of integrated sample preparation and detection is imperative for environmental or otherwise complex samples since a variety of contaminants can inhibit PCR amplification. Manual purification could be more efficient and/or effective than our chip-based DNA purification, but is more time consuming and less portable than the automated system in our device.

4.2 ELECTROLYTIC HYDRAULIC MICROPUMP

The efforts in investigating alternative methods of fluid handling resulted in an improved EHP design that could deliver a wide range of flow rates ($1.25 \mu\text{L}/\text{min}$ to $30 \mu\text{L}/\text{min}$) that was compatible with a variety of aqueous buffers and organic solvents (water, PBS, and ethanol). Pumps were fabricated entirely from polymeric materials (polystyrene and PDMS), suggesting the feasibility of low-cost, high throughput manufacturing. In addition, an electronic module was developed to deliver precise pumping voltages under software control. Fluid flow rates were directly proportional to the applied voltage, making it possible to roughly predict control pumping parameters. During sustained pumping, variability of approximately 10% was observed in the fluid flow rate,

especially at rates higher than 5 μ L/min. Precise pumping rates important for many microfluidic devices and it is clear that opportunities exist to establish a feed back control to regulate the voltage applied to the system.

We have demonstrated that EHPs can provide the necessary fluid flow rates and pressures for microfluidic analytical systems. The polymer-based fabrication methods are compatible with standard microfabrication technologies, making it possible to directly integrate these pumps with lab-on-a-chip systems. While the stainless steel electrodes were adequate, the integration of the gold electrodes allowed us to develop a more integrated manufacturing approach to the system.

4.3 INTEGRATED FLOW CYTOMETER

Controlled manipulation of the vertical position of a focused sample was achieved by tuning the flow-rates of the upper and lower focusing fluids. The manifold was fabricated by standard replica molding techniques and can be readily integrated into lab on-a-chip devices for applications. In particular, the ability to control the vertical position of a focused sample - on the fly - presents opportunities for creating optofluidic devices in which the alignment between the sample and the optical detection system is adjusted by tuning the flow-rates of the focusing fluids. If desired, control over the entire xy-space defined by the microchannel should be possible by adjusting, in addition to U_3/U_2 , the ratio of the rate of the focusing fluid from one side of the main channel relative to the rate of the focusing fluid from the other side of the channel. Ultimately, we anticipate this manifold will be used in portable biosensor instruments that accept fresh disposable LOCs with an automated optical alignment procedure.

An integrated flow cytometer was developed which contains integrated into a single Lab-on-a-chip two key components: a microfluidic focusing manifold and an integrated optical. Counting of non-fluorescent microspheres of 2- μ m size was demonstrated by triggering off the scattered light signal or, alternatively, by the fluorescence signal. An experiment was performed in which the ratio of the upper to the lower focusing fluids was swept to maneuver the bead stream from the top to the bottom of the microchannel. The count-rates were highest when the focusing ratio, U_3/U_2 , was near one, as we would expect based on our previous confocal microscopy experiment that was used to characterize the position of the focused stream in the hydrodynamic focusing manifold. This implies that the results obtained by simulation and confocal microscopy for

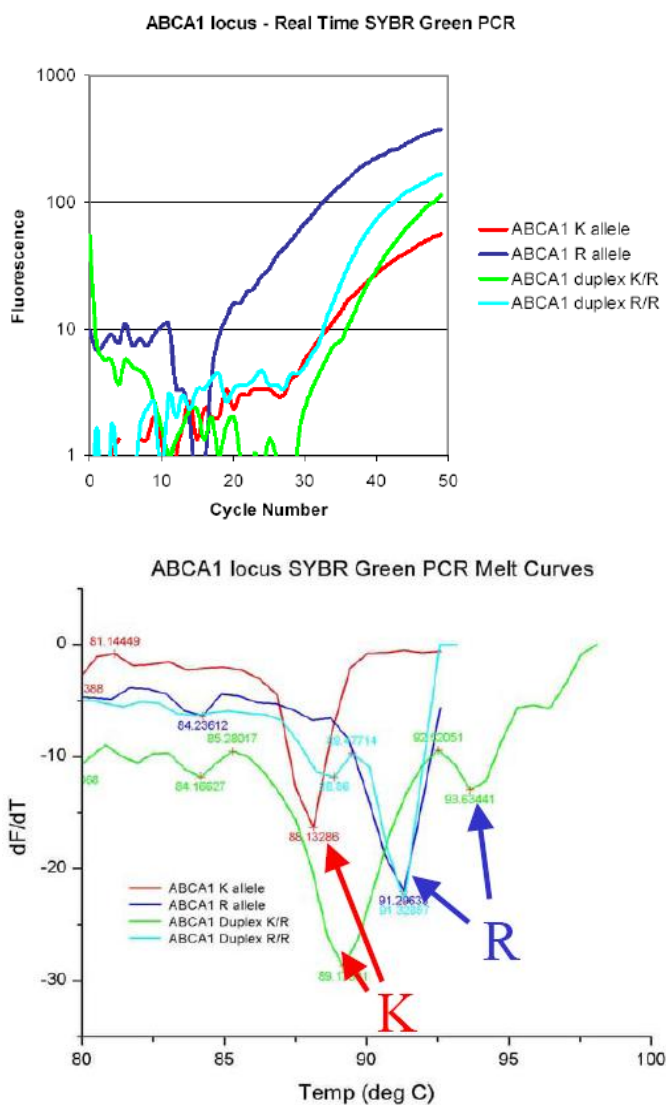


Figure 31 Real-time PCR detection of SNPs at the human ABCA1 locus. The top panel shows microchip-based real-time amplification of the different alleles at the ABCA1 locus. The bottom panel shows melting curve analysis of these reactions and successful discrimination between the alleles in the duplex assay.

characterizing the position of chromophore molecules dissolved in water can be extended to predict the position of micron-sized beads.

An allele-specific hybridization assay was developed in which microspheres were modified to contain ssDNA specific to either of two target sequences differing by only a single nucleotide. The target sequences contained spectrally independent chromophores and were mixed together into a heterogeneous dna mixture. A cocktail of beads were added to the mixture and allowed to hybridize, and then the beads were imaged with confocal microscopy. The microscopy images reveal successful specific hybridization of DNA at room temperature even for sequence differences of one nucleotide. Mixtures of the beads containing hybridized fluorescently-labeled DNA were pumped into our microfabricated flow cytometer but we were unable to successfully resolve the two species based on our optical signal (**Figure 28**). However, we were able to distinguish between red and green microspheres volume-loaded with fluorescent dye (**Figure 4**). We believe this limitation in spectral sensitivity is due to insufficient development of the signal conditioning and signal processing components of our integrated flow cytometer system. Specifically, differentiation between species is best achieved by comparing pulse area as opposed to pulse height [27]. Presently, our system works by recording voltage traces at the output of the photodetectors and then measuring the height of each pulse with MATLAB. It is not possible with our current system to measure the area of each pulse because the speed of the analog-to-digital converter (40-kHz) does not allow for a sufficient number of measurements during the time of a pulse. In addition, performing digital processing techniques on the complete voltage trace is computationally prohibitive due to its large size in memory. An improved flow cytometer on a chip must therefore contain advanced data acquisition and signal processing systems in order to differentiate between species.

Notably, emerging molecular probes present an additional potential avenue by which optical detection challenges may be overcome. Quantum dots are particularly promising for this problem because of their large optical absorption cross-section. In addition, recently there has been an interest in acquiring flow cytometric measurements of Raman Spectra in order to achieve higher multiplexability [81]. These next-generation flow cytometers will require the most advanced of data acquisition and electronic signal processing systems.

4.4 QUANTUM DOT MOLECULAR BEACONS

This research effort demonstrates that molecular beacons can be synthesized using QDs as a fluorophore and both organic and inorganic moieties as quenchers. Moreover, these results compare the relative effectiveness of two different binding chemistries for QD molecular beacon synthesis. For this research effort, we used two different methods to attach molecular beacon DNA to semiconductor QDs: 1) covalent linkage of amino-labeled DNA to carboxylated QDs (carboxyl-linked) and 2) linkage of biotinylated DNA to streptavidin-modified QDs (streptavidin-linked). Both of these methods have been demonstrated previously for attachment of DNA to QDs, but the two methods have not been quantitatively compared within a single study. We observed that the linkage method used had measurable effects on the properties of the molecular beacons. As shown in **Figure 29**, DNA hybridization-based unquenching of QD molecular beacons yielded larger increases in fluorescence for carboxyl-linked beacons (3.3-fold) than for streptavidin-linked beacons (2.1-fold) when using the same quencher (Iowa Black FQ). This fluorescence increase was mediated by binding of the molecular beacon DNA to single-stranded DNA that was perfectly complementary to the loop region. The difference between the carboxyl-linked and streptavidin-linked molecular beacons could be due to several reasons. First, there could be differences in the number of molecular beacon DNA hairpins attached to the two types of QDs. This could be due to differences in binding efficiency between the two linkage methods and the number of accessible reactive groups (carboxyl or streptavidin) on the QDs. Close packing of molecular beacon DNA on the surface of the QDs could interfere with secondary structure hairpin formation. This could result in inefficient quenching of the QD molecular beacon (in the absence of target) and result in a smaller change in fluorescence intensity during hybridization to target DNA.

Another difference between the two linkage strategies is the relative distance of the molecular beacon DNA (and therefore the quencher) from the core of the QD. Carboxyl-modified QDs were measured to have an average diameter of 7 nm while streptavidin-modified QDs had an average diameter of 13.5 nm. The difference in diameter is due to the large streptavidin protein molecules that are bound to the surface of the streptavidin-modified QDs. Using large proteins as spacers on the surface of the QD greatly increases the distance between the core of the QD and the quencher molecule, a parameter that is critical to FRET-based quenching. The Förster Radii (R_0) for the QD - Iowa Black FQ pair and the QD - dabcyI pair were calculated to be 5.0 nm and 4.1 nm, respectively. These represent the distances at which FRET efficiency is approximately 50%. Using the average measured diameter for carboxyl-modified and streptavidin-modified QDs, it is clear that the closest possible distance between the center of the QD and the quencher molecule would be 3.5 and 6.75 nm, respectively. From FRET efficiency calculations, distances greater than 5 nm from the center of this QD should result in less than 50% FRET efficiency. In fact, based on their measured diameter, it can be estimated that the carboxyl-modified QD - Iowa Black interaction would have a maximum FRET efficiency of 89% while the streptavidin-modified QD - Iowa Black interaction would have a maximum FRET efficiency of only 14%. Although these values would change relative to the exact number of quencher molecules associated with each QD, this demonstrates that FRET-based quenching of QDs is highly dependent upon the distance of the quencher from the QD. Therefore, the differences in between covalently-linked and streptavidin-linked QD molecular beacons could be dependent upon their initial quenched state. If the covalently-linked molecular beacons were initially better quenched than the streptavidin-linked molecular beacons, then hybridization-based unquenching would be more pronounced for the covalently-linked molecular beacons.

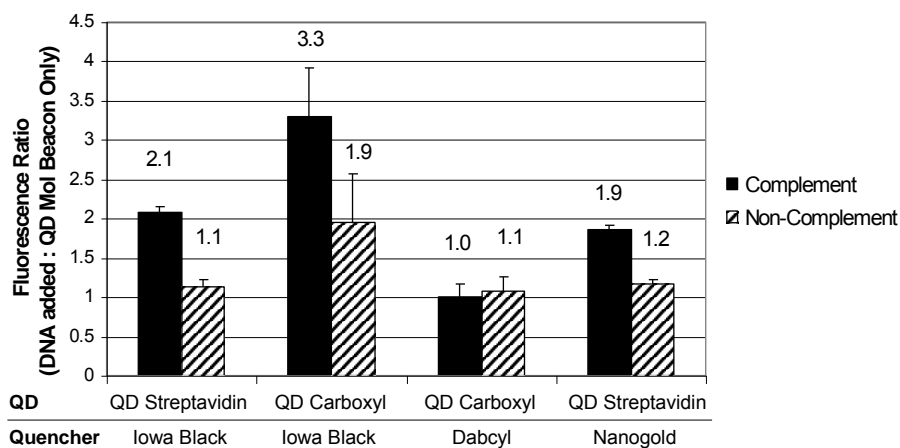


Figure 32 DNA hybridization-based unquenching of QD molecular beacons.

Approximately 2 pmol of QD molecular beacons were mixed with either 200 pmol of complement DNA (MB comp) or 200 pmol of non-complement DNA (invAF2). For each measurement, the fluorescence intensity of the mixture was normalized to the fluorescence intensity of 2 pmol of QD molecular beacons in PBS buffer only. These values are expressed as fluorescence ratios (QD MB with target DNA : QD MB with buffer only). These data represent the average of three separate measurements for each QD molecular beacon and error bars represent one standard deviation.

In addition to comparing linkage methods we also compared the effectiveness of different quencher moieties. We compared the dark quencher Iowa Black FQ with both dabcyI and 1.4 nm Nanogold particles. DabcyI has been used previously to create QD molecular beacons through carboxyl linkage [41]. Other groups have used gold nanoparticles to quench QDs through a variety of attachment methods [63, 82]. Gueroui and co-workers demonstrated that modifying the spatial separation between 1.4 nm Nanogold and a 522 nm QD (Qdot Corporation) resulted in varying quenching efficiencies. At a distance of 10 nm, the QD was quenched 20% while distances of 7.5 nm and 5.9 nm quenched the QD 50% and 80%, respectively. For our study, we attached both dabcyI and Iowa Black FQ quenched molecular beacons to carboxyl-linked QDs and also attached 1.4 nm Nanogold molecular beacons to streptavidin-linked QDs. To directly compare these quenchers, we mixed the QD molecular

beacons with both complement and non-complement DNA and measured their fluorescent intensity (**Error! Reference source not found.**). These data showed that Iowa Black FQ molecular beacons yielded a maximum increase in fluorescence of 3.3-fold; however, dabcy1 molecular beacons did not show any relative increase in fluorescence during target DNA hybridization. These data differ from a previous report by Kim, et al, where dabcy1 was used for successful QD quenching. Kim and co-workers, however, used 490 nm QDs that have considerably better spectral overlap with the absorbance maximum of the dabcy1 quencher. Therefore, the quenching efficiency of the dabcy1 quencher for the 490 nm QDs used by Kim and co-workers is expected to be much higher. Figure 5 shows the calculated spectral overlap of these QD-quencher pairs. As indicated in the spectra, Iowa Black FQ is a much better quencher for 525 nm QDs than dabcy1, due to the better overlap between the QD emission spectrum and quencher absorbance spectrum. The spectral overlap integral for the Iowa Black FQ – 525 nm QD interaction was calculated to be $2.6 \times 10^{-13} \text{ cm}^{-1}\text{M}^{-1}$, while that for the dabcy1 – 525 nm QD interaction was only $7.4 \times 10^{-14} \text{ cm}^{-1}\text{M}^{-1}$. This indicates that the Iowa Black FQ quencher is a significantly better quencher than dabcy1 when using 525 nm QDs.

For the 1.4 nm Nanogold quencher, we observed a 1.9-fold increase in fluorescence upon interaction with complementary DNA target. As described above, there may be some differences in quenching ability due to the linkage method used. Using the hydrodynamic radius measurements of the streptavidin modified QDs, the minimum separation distance between the 1.4 nm Nanogold particle and the QD, is approximately 7.5 nm. Gueroui and co-workers reported that, based on single molecule observations, a distance of 7.5 nm between a QD and Nanogold particle resulted in only 50% quenching efficiency.

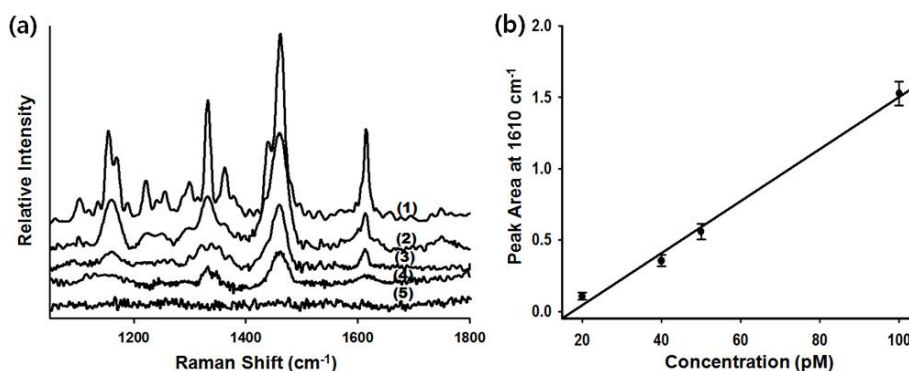


Figure 33: Effect of DNA Concentration on height of peak on Raman Spectrum.

This corresponds well to our data, in which there was nearly a two-fold increase in fluorescence intensity upon interaction with target DNA.

Finally, for any molecular sensing system, there must be specificity between target and non-target molecules. For each of the QD molecular beacons that were synthesized, specificity was determined by comparing hybridization with perfectly complementary DNA and non-complementary DNA. Regardless of the linkage method or the quencher moiety that was used, hybridization with complementary DNA yielded approximately 2-fold higher fluorescence intensity than hybridization with equal concentrations of non-complementary DNA. Dabcy1-quenched molecular beacons, however, did not exhibit changes in fluorescence for complementary or non-complementary DNA and the Nanogold-quenched beacons yielded only 1.6-fold higher intensity for complementary DNA. These data indicate significant specificity of the molecular beacons for the target DNA sequence and suggest that they could be used for discriminatory assays.

In summary, we have shown that QD molecular beacons are viable substrates for fluorescence-based DNA detection assays. We have also shown that a variety of attachment chemistries and quencher moieties can be used for QD molecular beacon synthesis. As expected, our data demonstrate that the spectral overlap of the QD fluorophore and the quencher directly affects the quenching efficiency of the molecular beacon. We have also shown that the QD to DNA linkage method has a direct effect on this efficiency. As with all FRET-based systems, the distance between the donor and acceptor must be tuned to provide the optimal efficiency for energy transfer.

These data outline the importance of choosing proper linkage methods and quencher moieties for creating high quality QD molecular beacons.

4.5 LIGASE DETECTION REACTION WITH SURFACE ENHANCED RAMAN DETECTION

We have reported the development of a novel SERS LDR system for the detection SNPs associated with mutations KRAS oncogene. Using SERS active LDR products related to KRAS cancer mutation, we successfully detected SERS signals with a limit of detection on the order of 20 pM and demonstrated the ability to quantify the solution concentration based on the intensity of the SERS emission. By relying on detection of the spectrally unique Raman fingerprint, rather than fluorescence emission this technique could increase the multiplexibility of current homogenous detection schemes by avoiding the problem of spectral overlap.

VI. DISSEMINATION OF RESEARCH FINDINGS

Peer-reviewed Publications

N. Cady, A.D. Strickland, C.A. Batt. Optimized linkage and quenching strategies for quantum dot molecular beacons. (2007) *Molecular and Cellular Probes*. 21(2): 116-124.

Y.S. Huh, A.J. Lowe, A.S. Strickland, C.A. Batt, D.E. Erickson. A Surface Enhanced Raman Scattering based Ligase Detection Reaction. (2009). *Journal of the American Chemical Society* 131(6): 2208-2213.

M.J. Kennedy, S.J. Stelick, S.L. Perkins, L. Cao, C.A. Batt. Hydrodynamic focusing with a microlithographic manifold: Controlling the vertical position of a focused stream. (Accepted) *Journal of Microfluidics and Nanofluidics* (In Press).

Conference Proceedings

C.A. Batt, N. Cady, S. Stelick, C. Lui, M.J. Kennedy, V.K. Koltko. Integrated nucleic acid based biosensor. MRS Fall 2006, Boston, MA.

N. Cady, V. Fusco, C.S. Lui, C.A. Batt. Development of PCR device for pathogen detection. Abstract of Papers, 232nd ACS National Meeting, San Francisco, CA, United States, 2006.

BIBLIOGRAPHY

1. Sachidanandam, R., Weissman D, Schmidt SC, Kakol JM, Stein LD, Marth G, Sherry S, Mullikin JC, Mortimore BJ, Willey DL, Hunt SE, Cole CG, Coggill PC, Rice CM, Ning Z, Rogers J, Bentley DR, Kwok PY, Mardis ER, Yeh RT, Schultz B, Cook L, Davenport R, et al., *A map of human genome sequence variation containing 1.42 million single nucleotide polymorphisms*. *Nature*, 2001. **409**(6822): p. 928-33.
2. Kidd, K., A. Pakstis, W. Speed, E. Grigorenko, S. Kajuna, N. Karoma, S. Kungulilo, J. Kim, R. Lu, A. Odunsi, *Developing a SNP panel forensic identification of individuals*. *Forensic Science International*, 2006. **164**: p. 20-32.
3. Sobrino, B., Brion, M., Carracedo, A., *SNPs in forensic genetics: a review on SNP typing methodologies*. *Forensic Science International*, 2005. **154**: p. 181-194.

4. Zhu, Y., David W. Hein, Mark A. Doll, Kristen K. Reynolds, Ntei Abudu, Roland Valdes, Jr and Mark W. Linder, *Simultaneous Determination N-Acetyltransferase-2 Single-Nucleotide Variations by Allele-Specific Primer Extension Assay*. *Clinical Chemistry*, 2006. **52**(6): p. 1033-39.
5. Perkel, J., *SNP genotyping: six technologies that keyed a revolution*. *Nature Methods*, 2008. **5**(5): p. 447-453.
6. Kim, S. and A. Misra, *SNP genotyping: Technologies and biomedical applications*. *Annual Review of Biomedical Engineering*, 2007. **9**: p. 289-320.
7. Mhlanga, M.M., Malmberg, L., *Using molecular beacons to detect single nucleotide polymorphisms with real-time PCR*. *Methods*, 2001. **25**(4): p. 463-471.
8. Socher, E., Jarikote, D.V., Knoll, A., Roglin, L., Burmeister, J., Seitz, O., *FIT probes: Peptide nucleic acid probes with a fluorescent base surrogate enable real-time DNA quantification and single nucleotide polymorphism discovery*. *Analytical Biochemistry*, 2008. **375**(2): p. 318-330.
9. Satterfield, B.C., Kulesh, D.A., Norwood, D.A., Wasteloski, L.P., Caplan, M.R. and J.A. West, *Tentacle Probes (TM): Differentiation of difficult single-nucleotide polymorphisms and deletions by presence or absence of a signal in real-time PCR*. *Clinical Chemistry*, 2007. **53**(12): p. 2042-2050.
10. Tian, H.H., A.F.R. Huhmer, J.P. Landers, *Evaluation of silica resins for direct and efficient extraction of DNA from complex biological matrices in a miniaturized format*. *Biochemistry*, 2000. **283**: p. 175-191.
11. Breadmore, M.C., K.A. Wolfe, I.G. Arcibal, W.K. Leung, D. Dickson, H. Feldman, P.M. Norris, J.P. Landers, *Microchip-based purification of DNA from biological samples, Microchip-based purification of DNA from biological samples*. *Analytical Chemistry*, 2003. **75**: p. 1880-1886.
12. Cady, N.C., S. Stelick, C.A. Batt, *Nucleic acid purification using microfabricated silicon structures*. *Biosensors and Bioelectronics*, 2003. **19**: p. 59-66.
13. Giordano, B.C.F., J. Ferance, S. Swedberg, A.F.R. Huhmer, J.P. Landers, *Polymerase chain reaction in polymeric microchips DNA amplification in less than 240s*. *Analytical Biochemistry*, 2001. **291**: p. 124-132.
14. Lin, Y.H., M. Huang, K. Young, T. Chang, C. Wu, *A rapid micropolymerase chain reaction system for hepatitis C virus amplification*. *Sensors and Actuators*, 2000. **71**: p. 2-8.
15. Schneegass, I., Kohler, J.M., *Flow-through polymerase chain reactions in chip thermocyclers*. *Rev. Mol. Biotechnol.*, 2001. **82**: p. 101-121.
16. Liu, R.H., J. Yang, R. Lenigk, J. Bonanno, P. Grodzinski, *Self-contained, fully integrated biochip for sample preparation, polymerase chain reaction amplification, and DNA microarray detection*. *Analytical Chemistry*, 2004. **76**: p. 1824-1831.
17. Unger, M.A., H.P. Chou, T. Thorsen, A. Scherer, S.R. Quake, *Monolithic microfabricated valves and pumps by multilayer soft lithography*. *Science*, 2000. **288**: p. 113-116.
18. Yokoyama, Y., M. Takeda, T. Umemoto, T. Ogushi, *Thermal micropumps for a loop-type micro channel*. *Sensors and Actuators*, 2004. **111**: p. 123-128.
19. Min, J.Y., E.F. Hasselbrink, S.J. Kim, *On the efficiency of electrokinetic pumping of liquids in nanoscale channels*. *Sensors and Actuators B*, 2004. **98**: p. 368-377.
20. Bretchel, R., W. Hohmann, H. Rudiger, H. Watzig, *Control of the electroosmotic flow by metal-salt-containing buffers*. *Journal of Chromatography A*, 1995. **716**: p. 97-105.
21. McClain, M.A., CT Culbertson, SC Jacobson, JM Ramsey, *Flow Cytometry of Escherichia coli on Microfluidic Devices*. *Analytical Chemistry*, 2001. **73**(21): p. 5334-5338.
22. Holmes, D., JK She, PL Roach, H Morgan, *Bead-based immunoassays using a micro-chip flow cytometer*. *Lab on a Chip*, 2007. **7**(8): p. 1048-1056.
23. Fu, A.Y., C Spence, A Scherer, FH Arnold, SR Quake, *A microfabricated fluorescence-activated cell sorter*. *Nature Biotechnology*, 1999. **17**(11): p. 1109-1111.
24. Wolff, A., I. R. Perch-Nielsen, U. D. Larsen, P. Friis, G. Goranovic, C. R. Poulsen, J. P. Kutter and P. Telleman, *Integrating advanced functionality in a microfabricated high-throughput fluorescent-activated cell sorter*. *Lab on a Chip*, 2003. **3**(1): p. 22-27.
25. Steinkamp, J.A., et al., *A new multiparameter separator for microscopic particles and biological cells*. *Rev. Sci. Instrum.*, 1973. **44**(5): p. 1301.
26. Steinkamp, J.A., R.C. Habbersett, and R.D. Hiebert, *Improved multilaser/multiparameter flow cytometer for analysis and sorting of cells and particles*. *Rev. Sci. Instrum.*, 1991. **62**(11): p. 2751-2764.
27. Zilmer, N.A., et al., *Flow Cytometric Analysis Using Digital Signal Processing*. *Cytometry*, 1995. **20**: p. 102-117.
28. Grimaldi, D., A. Palumbo, and S. Rapuano, *Hardware and software improvements in flow cytometry measurements*. *Measurement*, 2004. **36**: p. 111-119.

29. Engh, G.v.d. and W. Stokdijk, *Parallel Processing Data Acquisition System for Multilaser Flow Cytometry and Cell Sorting*. Cytometry, 1989. **10**.
30. Knight, J.B., A Vishwanath, JP Brody, RH Austin, *Hydrodynamic focusing on a silicon chip: Mixing nanoiters in microseconds*. Physical Review Letters, 1998. **80**(17): p. 3863.
31. Nieuwenhuis, J.H., J. Bastemeijer, P. M. Sarro and M. J. Vellekoop, *Integrated flow-cells for novel adjustable sheath flows*. Lab on a chip, 2003. **3**: p. 56-61.
32. Chang, C.-C., Huang, Z-X., Yang, R-J., *Three-dimensional hydrodynamic focusing in two-layer polydimethylsiloxane microchannels*. Journal of Micromechanics and Microengineering, 2007. **17**(8): p. 1479-1486.
33. Mao, X., Waldeisen, J.R., Huang, T.J., *"Microfluidic Drifting" - implementing three-dimensional hydrodynamic focusing with a single-layer planar microfluidic device*. Lab on a Chip, 2007. **7**: p. 1260-2.
34. Edenberg, H., D. Dick, X. Xuei, H. Tian, L. Almasy, L. Bauer, R. Crowe, A. Goate, V. Hesselbrock, K. Jones, *Variations in GABRA2, Encoding the $\alpha 2$ Subunit of the GABAA Receptor, Are Associated with Alcohol Dependence and with Brain Oscillations*. The American Journal of Human Genetics, 2004. **74**: p. 705-714.
35. Hohng, S., T. Ha, *Single-molecule quantum-dot fluorescence resonance energy transfer*. Chem Phys Chem, 2005. **6**: p. 956-60.
36. Willard, D.M., A. Van Orden, *Quantum Dots: resonant energy-transfer sensor*. Nature Materials, 2003. **2**: p. 575-6.
37. Liu, X., W. Farmerie, S. Schuster, W. Tan, *Molecular beacons for DNA biosensors with micrometer to submicrometer dimensions*. Analytical Biochemistry, 2000. **283**: p. 56-63.
38. Robelek, R., L. Niu, E.L. Schmid, W. Knoll, *Multiplexed hybridization detection of quantum dot-conjugated DNA sequences using surface plasmon enhanced fluorescence microscopy and spectrometry*. Analytical Chemistry, 2004. **76**: p. 6160-5.
39. Epstein, J., I. Biran, D.R. Walt, *Fluorescence-based nucleic acid detection and microarrays*. Anal Chimica Acta, 2002. **469**: p. 3-36.
40. Medintz, I.L., A.R. Clapp, H. Mattoussi, E.R. Goldman, B. Fisher, J.M. Mauro, *Self-assembled nanoscale biosensors based on quantum dot FRET donors*. Nature Materials, 2003. **2**: p. 630-8.
41. Kim, J.H., D. Morikis, M. Ozkan, *Adaptation of inorganic quantum dots for stable molecular beacons*. Sensors and Actuators B, 2004. **102**: p. 315-9.
42. Tan, L., Li Y., Drake T.J., Moroz L., Wang K., Li J. et al., *Molecular beacons for bioanalytical applications*. Analyst, 2005. **130**: p. 1002-5.
43. Vet, J.A., Marras, S.A., *Design and optimization of molecular beacon real-time polmerase chain reaction assays*. Methods Mol. Biol, 2005. **288**: p. 273-290.
44. Tyagi, S., F.R. Kramer, *Molecular beacons: probes that fluoresce upon hybridization*. Nature Biotechnology, 1996. **14**: p. 303-8.
45. Tsourkas, A., Behlke M.A., Rose S.D., Bao G., *Hybridization kinetics and thermodynamics of molecular beacons*. Nucleic Acids Research, 2003. **31**: p. 1319-1330.
46. Kristensen, V.N., et al., *High-Throughput Methods for Detection of Genetic Variation*. Biotechniques, 2001. **30**(2): p. 318-333.
47. Khanna, M., et al., *Multiplex PCR/LDR for detection of K-ras mutations in primary colon tumors*. Oncogene, 1999. **18**(1): p. 27-38.
48. Fang, C., et al., *DNA detection using nanostructured SERS substrates with Rhodamine B as Raman Label*. Biosensors and Bioelectronics, 2008. **24**(2): p. 216-221.
49. Qian, X., X. Zhou, and S. Nie, *Surface-Enhanced Raman Nanoparticle Beacons Based on Bioconjugated Gold Nanocrystals and Long Range Plasmonic Coupling*. Journal of the American Chemical Society, 2008. **130**(45): p. 14934-14935.
50. Cao, Y.C., R. Jin, and C.A. Mirkin, *Nanoparticles with Raman Spectroscopic Fingerprints for DNA and RNA Detection*. Science, 2002. **297**(5586): p. 1536-1540.
51. Fabris, L., et al., *A Heterogeneous PNA-Based SERS Method for DNA Detection*. Journal of the American Chemical Society, 2007. **129**(19): p. 6086-7.
52. Wabuyele, M.B. and T. Vo-Dinh, *Detection of Human Immunodeficiency Virus Type 1 DNA Sequences Using Plasmonic Nanoprobes*. Analytical Chemistry, 2005. **77**(23): p. 7810-5.
53. Jung, H.Y., et al., *Surface enhanced Raman scattering rom layered assemblies of close-packed gold nanoparticles*. Anal Chim Acta, 2007. **602**(2): p. 236-43.
54. Graham, D., et al., *Control of enhanced Rman scattering using a DNA-based assembly process of dye-coded nanoparticles*. Nature Nanotechnology, 2008. **3**(9): p. 548-551.

55. Barany, F., *Genetic disease detection and DNA amplification using loned thermostable ligase*. Proceedings of the National Academy of Sciences of the United States of America, 1991. **88**(1): p. 189-193.
56. Huh, Y.S., Lowe, A., Strickland, S., Batt, C.A., Erickson, D.,, *A Surface Enhanced Raman Scattering based Ligase Detection Reaction*. Journal of the American Chemical Society, 2009. **131**(6): p. 2208-2213.
57. Xia, Y., Whitesides, G.M., *Soft Lithography*. Angew. Chem. Int. Ed., 1998. **37**: p. 550-575.
58. Dasgupta, P.K., Eom, I., Morris, K.J., Li, J., *Light emitting diode-based detectors absorbance, fluorescence, and spectroelectrochemical measurements in a planar flow-through cell*. Analytical Chimica Acta, 2003. **500**: p. 337-364.
59. Dickinson, M.E., et al., *Multi-spectral imaging and linear unmixing add a whole new dimension to laser scanning fluorescence microscopy*. Biotechniques, 2001: p. 1272-1278.
60. Xu, H., Sha MY, Wong EY, Uphoff J, Xu Y, Treadway JA, Truong A, O'Brien E, Asquith S, Stubbins M, Spurr NK, Lai EH, Mahoney W, *Multiplexed SNP genotyping using the Qbead system: a quantum dot-encoded microsphere-based assay*. Nucleic Acids Research, 2003. **31**(8).
61. Vaidya, S.V., M. Lane Gilchrist, Charles Maldarelli, and Alexander Couzis, *Spectral Bar Coding of Polystyrene Microbeads Using Multicolored Quantum Dots*. Analytical Chemistry, 2007. **79**(22): p. 8520.
62. Du, H., Strohsahl, C.M., Camera, J., Miller, B.L., Krauss, T.D., *Sensitiviy and specificity of metal surface-immobilized "molecular beacon" biosensors*. Journal of the American Chemical Society, 2005. **127**: p. 7932-40.
63. Gueroim, Z., Libchaber, A., *Single-molecule measurements of gold-quenched quantum dots*. Physical Review Letters, 2004. **93**: p. 166108.
64. Duberret, B., Calame, M., Libchaber, A.J., *Single-mismatch detection using gold-quenched fluorescent oligonucleotides*. Nature Biotechnology, 2001. **19**: p. 365-70.
65. Altschul, S.F., Gish W., Miller W., Myers E.W., Lipman, D.J., *Basic local alignment search tool*. Journal of Molecular Biology, 1990. **215**: p. 403-10.
66. Clapp, A.R., Medintz, I.L., Mauro, J.M., Fisher, B.R., Bawendi, M.G., Mattoussi, H., *Fluorescence resonance energy transfer between quantum dot donors and dye-labeled protein acceptors*. Journal of the American Chemical Society, 2004. **126**: p. 301-310.
67. Dougan, J.A., et al., *Enhanced oligonucleotide-nanoparticle conjugate stability using thioctic acid modified oligonucleotides*. Nucl. Acids Res., 2007. **35**: p. 3668-3675.
68. Gaffney, R., et al., *Novel Fluorescent Ligase Detection Reaction and Flow Cytometri Analysis of SYT-SSX Fusions in Synovial Sarcoma*. Journal of Molecular Diagnostics, 2003. **5**(2): p. 127-135.
69. Huh, Y.S., et al., *Enhanced on-chip SERS based biomolecular detection using electrokinetically active microwells*. Lab on a Chip, 2009. **9**: p. 433-439.
70. Lee, K.J. and K.A. Fossier, *Fabrication of Stable Metallic Patterns Embedded in Poly(dimethylsiloxane) and Model Applications in Non-Planar Electronic and Lab-on-a-chip Device Patterning*. Advanced Functional Materials, 2005. **15**(4): p. 557-566.
71. Huh, Y.S., et al., *Enhanced on-chip SERS based biomolecular detection using electrokinetically active microwells*. Lab Chip, 2009: p. In press.
72. Venkateswarlu, V., Manjunath, K., *Preparation, characterization and in vitro release kinetics of clozapine solid lipid nanoparticles*. Journal of Controlled Release, 2004. **95**: p. 627-38.
73. O'Neal, D., Harrip, P., Dragicevic, G., Rae, D., Best, J.D., *A comparison of LDL size determination using gradient gel electrophoresis and light-scattering methods*. Journal of Lipid Research, 1998. **39**: p. 2086-90.
74. Pazy, Y., Laitinen, O.H., Ravoy, B., Kulomaa, M.S., Wilchek, M., Bayer, E.A., et al., *Crystallization and preliminary X-ray analysis of W120 K mutant of streptavidin*. Acta Crystallography D, 2001. **57**: p. 1885-6.
75. Tuan, V.-D., *Nanobiosensing using plasmonic nanoprobos*. Selected Topics in Quantum Electronics, IEEE Journal of, 2008. **14**(1): p. 198-205.
76. Hering, K., et al., *SERS: a versatile tool in chemical and biochemical diagnostics*. Anal Bioanal Chem, 2008. **390**(1): p. 113-24.
77. Jackson, J.B., et al., *Controlling the surface enhanced Raman effect via the nanoshell geometry*. Applied Physics Letters, 2005. **87**(3).
78. Chaney, S.B., et al., *Aligned silver nanorod arrays produce high sensitivity surface enhanced Raman spectroscopy substrates*. Applied Physics Letters, 2005. **87**(3).
79. Mahajan, S., et al., *Reproducible SERRS from structured gold surfaces*. Phys Chem Chem Phys, 2007. **9**(45): p. 6016-6020.
80. Faulds, K., et al., *Quantitative Simultaneous Multianalyte Detection of DNA by Dual-wavelength Surface-Enhanced Resonance Raman Scattering*. Angewandte Chemie, 2007. **9**(45): p. 1861-3.

81. Watson, D.A., et al., *A flow cytometer for the measurement of Raman spectra*. Cytometry A, 2008. **73A**: p. 119-128.
82. Dyadyusha, L., Yin, H., Jaiswal, S., Brown, T., Baumberg, J.J., Booy, F.P., et al., *Quenching of CdSe quantum dot emission, a new approach for biosensing*. Chemical Communications, 2005: p. 3201-3.